Combustion and Flame 179 (2017) 95–116

Contents lists available at ScienceDirect

Combustion and Flame

journal homepage: www.elsevier.com/locate/combustflame

Experimental investigation of turbulent flames in uniform dispersions of ethanol droplets

J. Kariuki*, E. Mastorakos

Hopkinson Laboratory, Engineering Department, University of Cambridge, CB2 1PZ, UK

ARTICLE INFO

Article history:
Received 31 July 2016
Revised 5 October 2016
Accepted 17 January 2017

Keywords:
Ethanol
PDA
PLIF
OH
CH_2O

ABSTRACT

A turbulent flame in an ethanol droplet-laden uniform mixture is investigated at overall equivalence ratios (ϕ_{ov}) of 0.62, 0.72 and 0.82, using a piloted Bunsen burner. Imaging of OH* chemiluminescence and simultaneous imaging of OH PLIF and Mie scattering, both at 5 kHz, and imaging of CH_2O-fuel PLIF at 5 Hz, were used to obtain instantaneous and time-averaged images, temporal sequences and 2-D estimates of flame surface density and curvature. 1-D PDA and LDA measurements were used to obtain droplet size and velocity statistics. At $\phi_{ov} = 0.62$, the flame takes a cylindrical shape, and changes to a cone shape with increasing fuel loading to obtain higher ϕ_{ov}. Larger droplets are generally observed to have lower average and RMS axial velocities than smaller droplets. Profiles of droplet size distributions indicate a decreasing droplet number density downstream together with a shift to larger droplet diameters. The flame structure is observed to be relatively smooth at locations near the burner exit, and becomes more contorted with distance downstream. In general, droplets are observed to coincide with low-to-intermediate regions of OH. Occasionally, droplets appear to penetrate the flame front, and are detected in regions of intermediate-to-high OH. This occurs particularly at the downstream locations where the flame closes across the jet, with no significant averaged droplet penetration observed past 2 mm in the direction normal to the flame front. Measurements show a gradual reduction in flame surface density and higher flame front curvature with both distance downstream and increasing fuel loading. Estimates of the average droplet evaporation rate increase with both distance downstream and ϕ_{ov}, as droplets appear in higher mean progress variable regions. The measurements reported here are useful for model validation of flame propagation in dilute sprays.

1. Introduction

Flame propagati on in droplet-laden mixtures is of importance to a variety of practical applications, such as direct-injection IC engines and in gas turbines. A better understanding of flames in multi-phase flows is crucial to the development of more efficient combustion-based technologies, and the topic continues to be of interest. Crucially, detailed experimental measurements are required to validate advanced numerical models to facilitate the development of new technologies. Detailed reviews of the key studies in this field are available in the literature [1–4], and this section briefly summarises some key investigations pertinent to the present work, which concerns the canonical problem of a turbulent flame propagating in, or stabilised against an incoming flow of, a uniform dispersion of fuel droplets.

An early experimental study by Burgoyne and Cohen [5] investigated laminar flame propagation in monodisperse tetralin fuel droplets suspended in an air mixture confined in a combustion tube. For droplet diameters below 10 μm, the air-droplet suspension was observed to behave like a vapour and a smooth flame front was observed. For droplet diameters above 40 μm, fuel droplets were observed to burn individually in their own envelope, promoting combustion by igniting adjacent droplets. At intermediate droplet diameters, a transitional combustion regime was observed. Such studies gave a qualitative understanding of the effect of droplet size on combustion behaviour, and led researchers in search for more quantitative data, such as in the experiments by Hayashi et al. [6]. In their study, burning velocities in monodisperse ethanol-air mixtures were measured. Observations showed that for large enough droplet diameters, the burning velocity of a droplet-vapour-air mixture exceeded that of a homogeneous

* Corresponding author.
E-mail address: james.kariuki@cantab.net (J. Kariuki).

http://dx.doi.org/10.1016/j.combustflame.2017.01.014

mixture of the same overall fuel-air ratio. Similar observations of the effect of droplet size on flame propagation were reported in [5], where the rugged and thickened flame structure observed for large droplet size conditions was suggested to result from incomplete droplet evaporation in the preheat zone, with droplet evaporation continuing into the hot products region of the flame. The resulting increase in the effective volume of the thickened flame structure was then suggested to promote combustion and lead to the higher burning velocities measured.

Further experimental studies expanded knowledge of the effect of droplet size on flame propagation, such as that by Myers and Lefebvre [7]. Using different fuels to also study the influence of fuel chemistry, their measurements showed flame speeds for the fuels investigated to be inversely proportional to the Sauter Mean Diameter (SMD) for droplet diameters above a critical value. This led to the conclusion that for large droplet sizes, evaporation rates are controlling to the fraction of fuel vapourised and consequently the flame speed. Furthermore, an increase in the amount of fuel vapour present in the inter-droplet space was observed to promote flame propagation. For low fuel vapour fractions, the inter-droplet distance was observed to be controlling to the survival of burning individual droplets within diffusion flame envelopes, necessary to sustain flame propagation at these limiting conditions. These and similar studies [8–10] with DNS and experiments in other configurations showed the intricate effects of droplet size and evaporation (and consequently overall fuel-air and liquid-air ratios) on flame propagation in multi-phase flows.

In practical spray systems, the spray is not monodisperse and the diameter of the droplets varies. For simplicity, a polydisperse spray is often characterised by a single value, such as the SMD, based on which the propagation behaviour is described. However, the polydispersity of a spray has been shown to influence the flame location, flame temperature and combustion behaviour. In this analytical study of a polydisperse laminar opposed flow spray diffusion flame, a characteristic droplet size was shown to be insufficient to accurately describe flame propagation [11]. This was particularly significant at limiting conditions such as flame extinction where significant errors were shown to arise.

With the development of computational models for spray combustion, detailed numerical studies have provided useful information on spray flame propagation. One such study is that of Neophytou and Mastorakos [9] where simulations of laminar planar one-dimensional freely-propagating flames in spray mists with detailed chemistry were performed. Their results showed the equivalence ratio at the reaction zone, denoted as the effective equivalence ratio (ϕ_{eff}), to be less than the overall equivalence ratio (ϕ_{ov}), due to a delay associated with droplet evaporation. This led to a reduction in flame speed in the case of overall lean mixtures, whilst increasing the flame speed for overall rich mixtures and large droplets as ϕ_{eff} approaches stoichiometry. For the latter case, evaporation of droplets which survive past the flame front into the hot products region resulted in pyrolysis and the production of hydrogen and acetylene, which by diffusing upstream to the reaction zone would result in an increase in flame speed of the propagating front. This showed that locally rich regions in reacting sprays can be associated with higher flame speeds which promote global flame propagation. Further work by Neophytou et al. [12] investigating spark ignition in a uniform monodisperse turbulent spray with complex chemistry Direct Numerical Simulations showed the flame propagation mechanism to consist of the reacting front jumping between igniting droplet-scale flames, detail not easily observed from experiments.

More recent numerical studies continue to provide closer examination of flame-droplet interaction and flame propagation in droplet-laden mixtures in the presence of turbulence, such as in the studies by Wacks et al. [13,14]. Using Direct Numerical Simulations to study flame propagation in n-heptane droplet-air mixtures, both premixed and non-premixed modes were observed to occur simultaneously but in different locations in mixture fraction space. Increasing the droplet size and turbulence intensity increased the relative contribution of non-premixed combustion to the overall heat release. A thicker flame was observed in droplet-laden mixtures compared to the corresponding stoichiometric gaseous mixture. Droplets were reported to evaporate predominantly in the preheat zone, with some droplets penetrating the flame front and continue to evaporate in the burnt gas region, resulting in fuel vapour diffusing back towards the flame front. The combustion process in the gaseous phase was observed to occur predominantly in locally fuel-lean regions, with significant equivalence ratio fluctuations arising along the flame front. From investigating the flame displacement speed and its correlation with curvature and strain rate, similarities in the local flame propagation behaviour in droplet-laden and gaseous premixed flames were observed. These similarities were suggested to indicate the suitability of applying turbulent premixed combustion modelling techniques in describing flame propagation in droplet-laden mixtures.

Of particular relevance to the present work is the experimental study by Pichard et al. [15] investigating the evaporation behaviour of n-heptane droplets in a low turbulence carrier air flow using a piloted burner. The investigation studied the effects of (i) the overall equivalence ratio (ϕ_{ov} = 0.72, 0.79 and 0.87), (ii) droplet residence time in a prevaporization tube (t_{res} = 21 and 49 ms) and (iii) the initial spray droplet Sauter Mean Diameter (SMD = 10, 20 and 25 μm) on the average droplet vaporization rate (K). Droplet velocity and size information was obtained from PDA measurements, with mean progress variable ($\langle c \rangle$) data of the spray flame obtained using OH PLIF. Their observations showed K to increase with $\langle c \rangle$, and consequently with ϕ_{ov} at a given axial location due to a shorter flame, with K also increasing with SMD. An increase in t_{res}, for which the turbulence intensity of the reactants stream decreased, led to a reduction in K as the degree of premixing increased to achieve a globally leaner and longer flame. These results are particularly relevant to many practical applications employing spray flames, where some degree of prevaporization, and consequently premixing, generally occurs and for which the effects of droplet vaporization on the global flame behaviour are important. The use of their experimental results as validation data for computational simulations by [16], which showed good agreement of the general droplet and flame behaviour, further emphasises the necessity of such detailed experimental studies in the development of advanced spray combustion models.

The application of well developed turbulent premixed flame analysis methods to study spray combustion in these recent studies motivates the present work, where the focus is on partially prevaporized ethanol spray flames. In comparison to the field of turbulent premixed flames where a larger collection of data measuring parameters pertinent to flame structure and propagation (such as burning rates, displacement speeds, surface density, curvature statistics) are widely available [17], such information is not readily available for turbulent spray flames [18]. Additionally, the majority of the detailed work on flame structure and propagation in droplet-laden mixtures has focused on laminar flows, with few studies investigating turbulence effects in detail available in the literature [19–22]. The lack of data on the canonical problem of turbulent planar flame propagating in a uniform dispersion of droplets, which is fundamental to understanding spray flame stabilisation and important applications such as gas turbine relight, has been highlighted in a recent review article [23]. The application of laser diagnostics to obtain detailed measurements of spray flames in simple burner configurations, such as in [10,15,24], are crucial to better understanding flame structure and propagation in droplet-laden mixtures through providing new insights and

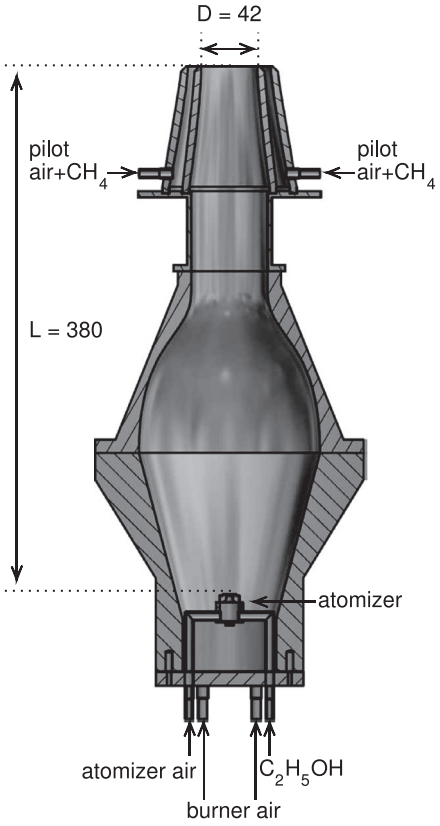

Fig. 1. Schematic of the piloted burner. All dimensions in mm.

validation data for computational simulations. The focus of the present work is to apply laser diagnostics to investigate, in detail, flame structure in a well defined droplet-laden mixture using a generic burner configuration borrowed from canonical turbulent premixed flame research. Flame analysis methods commonly used to study turbulent premixed combustion will be applied to characterise the partially prevaporized turbulent spray flames of this work, with the results also serving as validation data for computational studies of spray combustion in a canonical configuration.

2. Experimental methods

2.1. Apparatus and flow conditions

The spray burner was designed to provide a uniform mixture of air and fuel droplets, and a schematic of the burner is shown in Fig. 1. Air is supplied to the main burner section from the bottom, and passes through a flow condition section (not shown in Fig. 1) comprising of a perforated plate (4 mm diameter holes, approximately 40% open area) and packed with stainless steel ball bearings to flatten the velocity profile. Air and liquid ethanol fuel are supplied to a Delavan AL-06 air-assist external mix atomizer placed coaxially with the burner axis immediately downstream of the flow conditioning section. The atomizer air breaks the liquid sheet into a fine spray of droplets which are then carried upwards with the main burner air. The droplet-air mixture passes through a diverging section and then a converging section, to prevent liquid accumulation on the burner walls, before exiting the burner through a nozzle of inner diameter $D = 42$ mm at the exit plane. The inner diameter of the nozzle initially converges to a value of 41 mm at a location 4 mm upstream of the exit plane, before diverging along a chamfer to 42 mm. The distance from the atomizer to the exit plane is approximately 380 mm, and some degree of fuel vaporization is expected to occur inside the burner. Located at the burner exit is a ring pilot flame, fuelled with a premixed methane-air mixture, providing a continuous ignition source serving to stabilise a spray flame exposed to the lab atmosphere. No accumulation of ethanol fuel at the base of the burner was observed, indicating that any liquid deposited onto the burner walls due to droplet impact evaporated and mixed with the main flow prior to exiting the burner.

Ethanol fuel is metered using four Alaris IVAC syringe pumps, models P6000 and P7000, each with a maximum infusion rate of 20 ml/min. These are arranged in a parallel configuration and fitted with 60 ml capacity syringes. For the pilot flame, methane is provided from a pressurized cylinder and controlled using a flow rotameter (range 0–10 l/min). Air is supplied from a compressor line, with its temperature measured to be approximately 286 K at its inlet to the burner. Air for the atomiser and the pilot are controlled using flow rotameters (range 0–50 l/min and 0–100 l/min, respectively) and the main burner air is metered using an Alicat mass flow controller (range 0–1500 standard l/min). For all measurements reported in the present work, the flow rates of the atomiser and main burner air are fixed at 15 and 220 standard l/min, resulting in a bulk air velocity U_b of 2.83 m/s. The atomiser liquid flow rate, $\dot{Q}_f$, is set at 24.4, 28.4 and 32.4 ml/min to obtain ϕ_{ov} values of 0.62, 0.72, and 0.82, respectively, corresponding to power values of 9.6 kW, 11.1 kW, and 12.7 kW, respectively. The pilot air and methane fuel flow rates were fixed at 30 and 3.5 standard l/min and mixed upstream of the pilot to obtain a pilot flame of $U_{pilot} =$ 1.1 m/s, $\phi_{pilot} = 1.1$ and power = 1.9 kW. The ϕ_{ov} values reported for the spray flame do not take into account additional fuel from the rich pilot flame. As the overall power of the liquid fuel flame is 5–7 times that of the pilot flame, any significant effect of the pilot flame is likely to be felt only at small distances from the base of the spray flame. Based on this flow delivery system, U_b, ϕ_{ov}, U_{pilot} and ϕ_{pilot} are estimated to be uncertain to 3%, 2%, 5% and 7%, respectively.

2.2. PDA and LDA

A Spectra-Physics stabilite 2017 Argon-Ion laser is used as the light source for a Dantec FibreFlow system configured in a 1-D PDA and 1-D LDA setup to obtain droplet size and velocity measurements. The FibreFlow system performs colour separation of the 590 nm output of the Argon-Ion laser producing a pair of 488 nm beams and a second pair of 514.5 nm beams. These beams are steered to the transmitting probe using fibre-optic cables from which each beam exits with a diameter of approximately 1.5 mm and a spacing of 70 mm from its paired-beam. The transmitting probe was fitted with a 500 mm length focal lens, with a 60 μm iris used as an alignment target for the probe volume where the four beams intersect. The PDA receiving probe, fitted with a 310 mm focal length lens and a 100 μm aperture, was oriented at 30° with respect to the transmitting probe in the forward scattering configuration. The LDA receiving probe, fitted with a Micro Nikkor 105 mm (f/2.8) lens, was positioned directly opposite the transmitting probe to obtain droplet velocity measurements in the forward scattering mode. The PDA receiving probe was used to measure the axial velocity component together with the droplet size, and the LDA receiving probe used to measure the radial velocity component.

A single Bragg cell is used to shift the Doppler frequency of a single beam from each pair to 40 MHz. The transmitting and receiving optics were aligned to obtain satisfactory Doppler bursts and typical validation rates were approximately 80% for both the PDA and LDA measurements. Typical data rates of the PDA and LDA measurements acquired within the centre of the droplet-laden jet for the non-reacting case were approximately 2 kHz and 5 kHz,

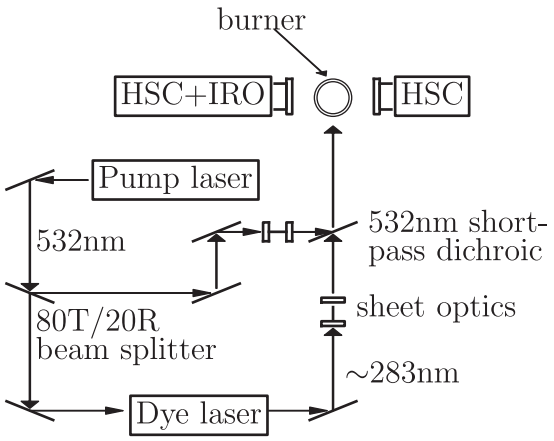

Fig. 2. Layout of the simultaneous OH PLIF and Mie scattering acquisition system.

respectively. The transmitting and receiving probes were mounted on a traverse system permitting translation in all three spatial directions. Droplet size and velocity measurements were obtained by traversing the optical system along the radial direction of the droplet-laden jet, at several axial locations ranging from 0.14*D* to 4*D*, where *D* is the burner exit diameter (42 mm). System control and data acquisition was performed using BSA Flow Software, with data acquisition at each probe location stopped when either 20,000 samples were recorded or an acquisition duration of 30 s had elapsed. The uncertainty estimates of the PDA and LDA measurements were not explicitly determined. However, repeated measurements of the droplet Sauter Mean Diameter (SMD) and time-averaged axial velocity ($\langle u \rangle$) for the same spray were performed and found to be within 3% and 1%, respectively. Conservative estimates of the experimental uncertainty of the PDA and LDA measurements presented in this work are approximated as 6% and 2%, respectively, which are within those reported in the literature [15].

2.3. Simultaneous OH PLIF and Mie scattering

Simultaneous measurements of OH PLIF and Mie scattering were performed using a fast response (5 kHz) laser diagnostic system to study the droplet-flame interaction behaviour. A schematic of the system is provided in Fig. 2. A single, high-repetition rate, diode solid state laser (model JDSU Q201-HD, 532 nm output, beam power of 14 W at 5 kHz, pulse length of 18 ns) was used as both the light source for Mie scattering measurements and as the pump laser for a fast OH dye laser system. A plate beam splitter was used to split the 532 nm beam, with approximately 20% of the beam power reflected to the Mie scattering sheet forming optics to obtain a laser sheet of approximately 40 mm height and 1 mm thickness. The remainder of the 532 nm beam transmitted through the plate beam splitter (approximately 80%) was steered to pump a high speed tunable dye laser (SIRAH Credo model 2400) to produce a beam at 566 nm using a Rhodamine 6G and ethanol dye solution. This was then frequency doubled using a BBO crystal to produce a beam with an average power of 240 mW at 5 kHz (48 μJ/pulse). The frequency doubled output was tuned near 283 nm to excite the $Q_1(6)$ line in the $A^1\Sigma$ - $X^2\Pi(1,0)$ band. The beam was then expanded into a sheet approximately 0.25 mm thick and of height 30 mm using various sheet forming optics. The two laser sheets were then combined using a 532 nm shortpass dichroic mirror and terminated after the burner with a beamdump. Alignment of the laser sheets was performed using burn paper, with the alignment uncertainty estimated at 0.1 mm.

Mie scattering images were acquired using a Photron SA1.1 monochrome high speed CMOS camera with 1024 × 1024 pixel resolution up to 5.4 kHz fitted with a Micro Nikkor 105 mm (f/2.8) lens and a 532 nm CWL, 10 nm FWHM, bandpass filter. The camera exposure duration was set at 9 μs at an imaging rate of 5 kHz. OH PLIF imaging was performed using a LaVision IRO high speed two stage intensifier with a spectral range of 190 to 800 nm coupled to an identical Photron SA1.1 high speed CMOS camera. The latter was fitted with a Cerco 2178 UV lens (f/2.8) and a UV bandpass filter (300–325 nm), with the intensifier gated at 400 ns at an imaging rate of 5 kHz. The OH and Mie imaging cameras were synchronised with the 532 nm output pump laser. A transparent target image with opaque markers was used to calibrate both cameras to the same imaging plane along which the laser sheets to excite PLIF of OH and cause Mie scattering of laser light off the fuel droplets were aligned to. Measurements with both cameras were acquired with an effective spatial resolution of 0.096 mm per pixel along the imaging plane, with the depth of field approximated as the laser sheet thickness of 0.25 mm and 1 mm for the OH and Mie images, respectively. For each flame condition, imaging was performed at five different regions separated axially, each of height of 30 mm, and complementing the PDA data obtained at axial locations up to 4*D* downstream of the burner exit. For each flame condition and imaging region, a set of 5000 images were acquired and stored for post processing.

2.4. OH* chemiluminescence

OH* chemiluminescence measurements were obtained using the imaging system described for the OH PLIF measurements, with a different UV bandpass filter (270–370 nm) fitted to the UV lens attached to the SA1.1 high speed camera. The two-stage intensifier coupled to the camera was gated at 190 μs at 5 kHz and measurements were acquired with an effective spatial resolution of 0.174 mm per pixel along the imaging plane. 5000 images were recorded for each flame condition and stored for post processing.

2.5. CH_2O-fuel PLIF

A Continuum Surelite-II 10 Nd:YAG laser fitted with a third harmonic generator was used to produce an output beam at 355 nm to excite the $A^2A_1 \leftarrow X_1A^1 4_0^1$ pQ transition of CH_2O. The beam was then expanded into a sheet of height and width of approximately 30 mm and 1 mm, respectively. CH_2O-fuel PLIF was captured using a Nanostar intensified CCD camera with 1280× 1024 pixel resolution, with the internal intensifier optimised to collect light in the visible range. The camera was fitted with a Micro Nikkor 105 mm (f/2.8) lens. A combination of GG 395 and BG 40 filters were used to create a bandpass filter (395–610 nm), which were fitted to the camera lens together with a 355 nm notch filter to prevent detection of laser light scattering off the fuel droplets. The intensifier was gated at 400 ns at 5 Hz, with 2 × 2 hardware binning implemented. Measurements were acquired with an effective spatial resolution of 0.116 mm per pixel along the imaging plane, with the depth of field approximated as the laser sheet thickness of approximately 1 mm. For each flame condition, imaging was performed at four different regions separated axially, each of height of approximately 30 mm, up to a distance 3.2*D* downstream of the burner exit. For each flame condition and imaging region, a set of 200 images were recorded and stored for post processing. At this excitation wavelength (355 nm), a non-reacting ethanol droplet-laden mixture was observed to fluoresce, indicating fluorescence directly from the fuel. This behaviour has also been reported in the literature [25], and cannot be easily subtracted from the CH_2O signal acquired for the reacting conditions. Therefore, the acquired signal is considered a combination of fluorescence of both ethanol fuel and CH_2O.

2.6. Data analysis

2.6.1. Simultaneous OH PLIF and Mie scattering

Each instantaneous raw image of OH PLIF and Mie scattering was initially filtered using a 2-D median non-linear filter for noise reduction, with a 3× 3 pixel filter size used. The signal-to-noise ratio, approximated as the ratio of the average signal to background intensity, for the OH PLIF measurements is approximately 21:1 just above the burner exit, decreasing along the flame to approximately 5:1 at the furthest downstream regions imaged. The signal-to-noise ratio for the Mie signal varied from approximately 170:1 just above the burner exit to approximately 9:1 at the furthest downstream regions imaged. The filtered images were then corrected for inhomogeneities in the laser sheet profiles. Identical reference points were selected on the target image from each camera and used to define a transformation matrix relating the coordinate sets on both cameras. This was used to match the coordinate set of the OH PLIF imaging plane to that of the Mie scattering imaging plane. The average deviation of the matched reference points after applying the coordinate transformation was calculated to be in the sub-pixel range. Using threshold values of pixel intensities determined qualitatively by trial and error, the corrected OH PLIF images were then converted into binary images to differentiate regions of burned and unburned gas. The instantaneous flame front edge was then defined as the boundary between these two regions on the condition that droplets are present on the reactants side of the flame edge superposed on the Mie image. An ensemble-average of the binary images for each data set was obtained to estimate a map of the mean progress variable ($\langle c \rangle$), with values ranging from 0 to 1 reflecting the probability of finding burned gases (0 = low, 1 = high). Each position along the flame edge could then be associated with a $\langle c \rangle$ value from the ensemble-averaged $\langle c \rangle$ map and used to obtain other pertinent data such as estimates of flame surface density.

2.6.2. 2-D flame surface density

One of the objectives of this work is to measure parameters commonly applied to describe turbulent premixed combustion to characterise the partially prevaporized ethanol spray flames of this study. One such statistic is the flame surface density (Σ) which describes wrinkling of the flame surface by turbulence, and has been shown to affect the local burning rate in premixed flames [26]. Following the methodology used by the present authors in an earlier study investigating turbulent methane premixed flames [27], two different methods were applied to obtain 2-D estimates of the three-dimensional flame surface area-to-volume ratio. These are (i) the flame length and flame zone area method by Shepherd [26], and (ii) the gradient of progress variable (∇c) method by Deschamps et al. [28]. These are briefly summarised here, and more detail on them can be found in [27] and [29]. In the method by Shepherd [26], the 2-D estimate of Σ is defined as

$$\Sigma(\langle c \rangle) = \frac{L(\langle c \rangle)}{A(\langle c \rangle)} \frac{1}{n_f} \tag{1}$$

where A and L are the flame zone area and flame length, respectively, as functions of the ensemble average progress variable $\langle c \rangle$, and n_f is the number of flame images analysed. This 2-D estimate of flame surface density has been shown to be a reasonable approximation of the true flame surface area-to-volume ratio [26].

In the second method by Deschamps et al. [28], the 2-D estimate of Σ is defined as

$$\Sigma = \left\langle \frac{\Sigma'_{xy}}{cos(\theta_{xy})} \right\rangle \tag{2}$$

where in this work, Σ'_{xy} is the magnitude of the gradient of the ensemble averaged progress variable $\nabla\langle c \rangle$, and θ_{xy} is the orientation of the flame front normal relative to the image plane. The latter is calculated as the inverse tangent of the quotient of the unit normal vectors of $\nabla\langle c \rangle$ in the x and y directions. The standard error of the flame surface density estimates using the method by Shepherd [26] and Deschamps et al. [28], with a 95% confidence interval, were evaluated to be approximately 1% and 2%, respectively. Considering errors arising from post-processing of the OH PLIF images, a conservative estimate of the experimental uncertainty of the Σ estimates based on the OH PLIF data is approximated as 4%. However, this is without consideration of errors arising from the imaging apparatus such as the non-linear pixel response of the CMOS camera which would affect the accuracy of the measurements obtained [30].

2.6.3. 2-D flame front curvature

2-D estimates of the flame front curvature were evaluated at each point along the instantaneous flame edge extracted from the binary OH PLIF images. Following the method described in [29,31], a filter length of 5 points was chosen, and the flame edges filtered using a zero-phase digital filter. With 's' denoting the flame front length measured from a fixed origin on the filtered edge, the curvature of the filtered flame edges were evaluated by calculating the first and second derivatives in the x and y directions along the flame edge with respect to s. The first and second derivative curves were also filtered using the same zero-phase digital filter. Estimates of the two-dimensional flame front curvature were then calculated using the following

$$\kappa = \frac{\dot{x}\ddot{y} - \dot{y}\ddot{x}}{(\dot{x}^2 + \dot{y}^2)^{3/2}} \tag{3}$$

where $\dot{x} = dx/ds$ and $\ddot{x} = d^2x/ds^2$, and similarly for y. The flame front is defined with the unit normals pointing towards the reactants. Therefore, the curvature is positive (negative) where the radius of curvature of the flame front is convex (concave) to the reactants. Estimates of the magnitude of the 2-D flame front curvature are limited by the thickness of the laser sheet used to excite OH radicals (approximately 0.25 mm) to 4 mm^{-1}. The standard error of the curvature measurements with a 95% confidence interval was evaluated to be within 3%. From previous work [27], the curvature of digitized circles of radius 0.23 mm were calculated to within an accuracy of 2% using the method describe above. In addition to considering errors arising from identifying the flame edge from the OH PLIF images, a conservative estimate of the experimental uncertainty of the κ measurements based on the OH PLIF data is approximated as 10%.

2.6.4. OH* chemiluminescence

As the average flame is axially symmetric, the ensemble average of the two-dimensional projection of the line-of-sight OH* chemiluminescence signal can be transformed using an inverse Abel transform to calculate the three-dimensional OH* chemiluminescence signal. The imaging area of the OH* chemiluminescence measurements extends from the burner exit to a distance 4D downstream. These measurements are useful for identifying the average flame shape, and complement the OH PLIF data which was acquired for separate axial regions of the flame at different time instances.

2.6.5. CH_2O-fuel PLIF

Following the image processing procedure implemented for the OH PLIF data, a 3× 3 pixel size 2-D median non-linear filter was initially applied to each raw CH_2O-fuel PLIF image for noise reduction. The signal-to-noise ratio, also approximated as the ratio of the average signal to background intensity, for the CH_2O-fuel PLIF measurements is approximately 12:1 just above the burner exit, decreasing along the flame to approximately 2:1 at the furthest downstream regions imaged. The filtered images were then

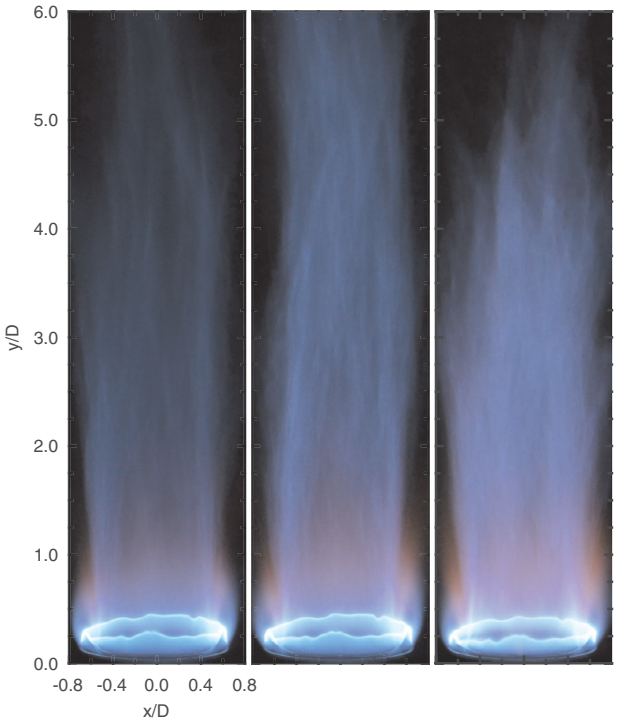

Fig. 3. Photographs of the spray flame at conditions ES1, ES2 and ES3 (left to right).

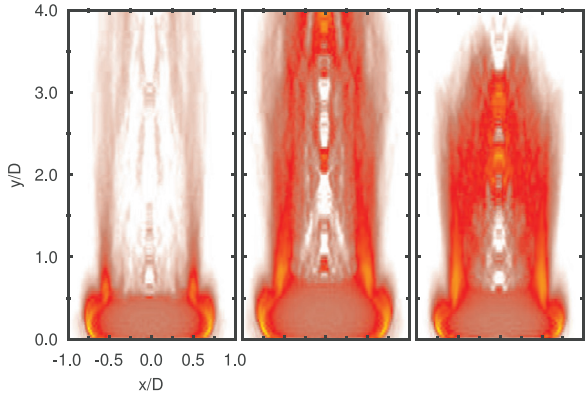

Fig. 4. Ensemble-average OH* chemiluminescence images, converted using an inverse Abel transform, of the spray flame at conditions ES1, ES2 and ES3 (left to right).

Table 1
Summary of experimental conditions. S_L is the laminar flame speed obtained from [32, Table 2]. δ_L is the laminar flame thickness (ν/S_L, $\nu = 1.45\times10^{-5}$).

Flame	U_b [m/s]	Q_f [ml/min]	ϕ	S_L [cm/s]	δ_L [mm]
ES1	2.83	24.4	0.62	10.4	0.139
ES2	2.83	28.4	0.72	19.3	0.075
ES3	2.83	32.4	0.82	28.0	0.052

corrected for inhomogeneities in the laser sheet profile. CH_2O-fuel PLIF imaging was performed at similar axial locations as that for the simultaneous OH PLIF and Mie scattering measurements to facilitate comparison of the data. Estimates of the 2-D flame surface density (Σ) and flame front curvature (κ) based on the CH_2O-fuel PLIF signal are also evaluated. With the flame edge defined as the boundary of the CH_2O-fuel PLIF signal, estimates of Σ are obtained by superposing the flame edge on the mean progress variable map evaluated from the binary OH PLIF images. Following the procedure described for the OH PLIF signal, estimates of Σ are obtained using the methods of Shepherd [26] and Deschamps et al. [28], Eqs. (1) and (2), respectively. The standard error of the Σ estimates based on the two methods are both approximately 5%. Estimates of κ as defined in Eq. (3) are also obtained, and calculated to have a standard error of approximately 10%. Considering errors arising from post-processing of the CH_2O-fuel PLIF images, conservative estimates of the experimental uncertainty of the Σ and κ values based on the CH_2O-fuel PLIF data are approximated as 10% and 15%, respectively.

3. Results

In this section, instantaneous and ensemble-averaged images, temporal sequences, 2-D estimates of flame surface density and flame front curvature, and droplet size and velocity data for the ethanol spray flame at conditions ES1, ES2 and ES3 ($\phi_{ov} = 0.62$, 0.72 and 0.82, respectively) are presented and discussed.

3.1. Average flame shape

Photographs of the ethanol spray flame at conditions ES1 to ES3 are shown in Fig. 3. Two distinct regions are observed in each photograph, the strong emission of the short pilot flame at the burner exit, and the weaker emission of the long spray flame. Both flames have a blue colour. As the fuel flow rate, Q_f, is increased, the emission of the spray flame increases, and its average length initially increases between conditions ES1 to ES2 before decreasing at condition ES3. The average reaction zone location is also revealed by the ensemble-averaged OH* chemiluminescence image, converted using an inverse Abel transform, shown in Fig. 4. At condition ES1, the majority of the reaction is observed to occur near the pilot flame, with a weak chemiluminescence signal detected downstream along the shear layer of the droplet-laden jet. The pilot flame extends a distance of approximately 0.2D, where D is the nozzle diameter at the exit. Very low chemiluminescence is observed near the burner axis at this condition, indicating that reaction is occurring predominantly along the shear layer. The average length of the flame extends past a distance 4D downstream of the burner exit, and the average flame shape is cylindrical. As Q_f is increased to condition ES2, a stronger chemiluminescence signal appears downstream of the pilot flame, and also towards the centre of the jet. The average shape of the spray flame has also changed to a resemble a cone, and the flame brush length has increased. The strong chemiluminescence signal observed at a downstream location of approximately 4D indicates the average location of the vertex of the cone-shaped flame where it closes across the droplet-laden jet. At condition ES3, the average length of the cone-shaped flame decreases to approximately 3.5D, and a stronger chemiluminescence signal is also detected downstream of the pilot, indicating a further increase in reaction, and heat release, of the spray flame.

3.2. Droplet velocity and diameter

Profiles of the time-averaged and RMS fluctuations of the axial velocity ($\langle u \rangle$ and u_{RMS}, respectively) and RMS fluctuations of the radial velocity (v_{RMS}) of the fuel droplets, each normalized by the bulk air velocity at the burner exit (U_b), and profiles of the droplet Sauter Mean Diameter (SMD) are presented in Fig. 5 for both reacting and non-reacting cases. The flow conditions for the non-reacting case are identical to those for condition ES3, and the experimental conditions are presented in Table 1. In each plot, profiles measured along the radial direction of the droplet-laden jet are presented for various axial locations downstream ranging

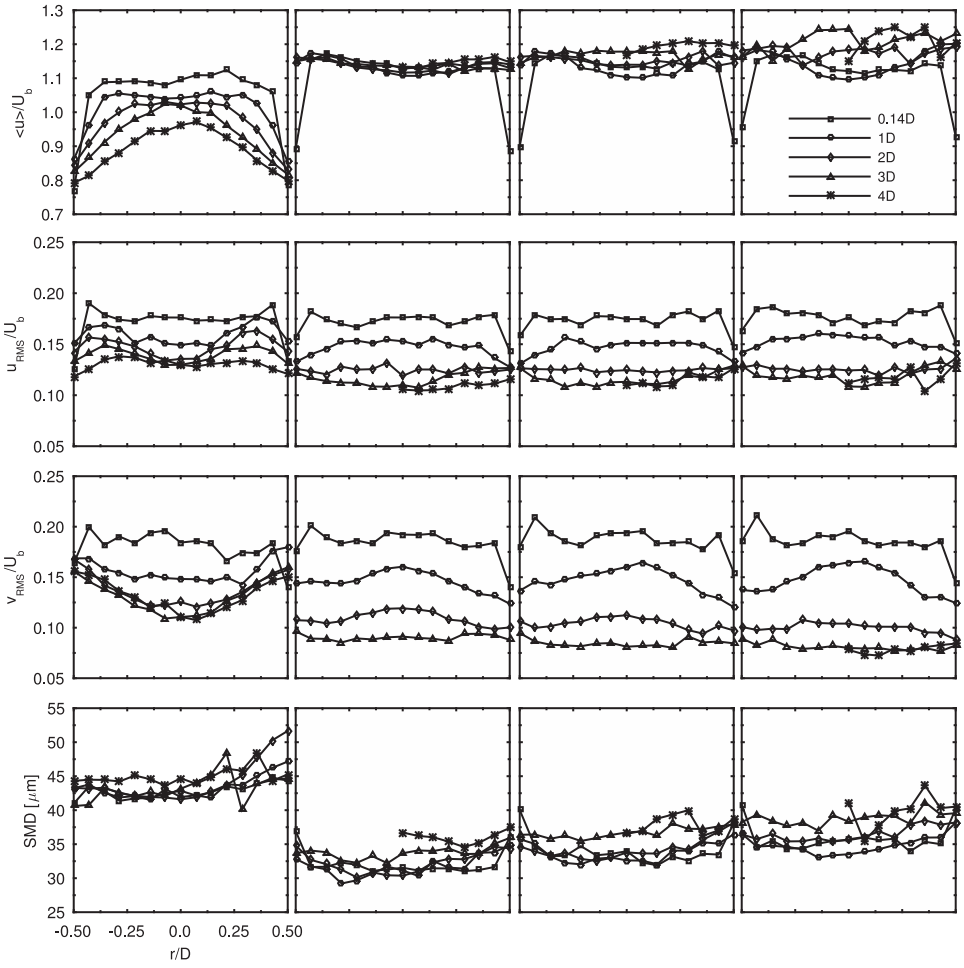

Fig. 5. Plots of $\langle u \rangle / U_b$, u_{RMS}/U_b, v_{RMS}/U_b and SMD (rows top to bottom) for a non-reacting case (ES3 with pilot off) and for the spray flame at conditions ES1, ES2 and ES3 (columns left to right).

from 0.14D to 4D from the burner exit. The non-reacting case is discussed first. Profiles of $\langle u \rangle$ take a near top-hat shape near the burner exit indicative of fully developed pipe flow. The axial velocity profiles then transition to a parabolic shape downstream as the jet spreads into the quiescent ambient, with values of $\langle u \rangle$ of the droplets near the centre of the jet decreasing with distance downstream. Values of u_{RMS} are observed to vary between $0.11U_b$ and $0.19U_b$, indicative of turbulent conditions within the droplet-laden mixture. The location of the shear layer can also be observed from the local peaks in the u_{RMS} profiles, particularly near the burner exit.

The largest magnitude of the mean radial velocity of the droplets $\langle v \rangle$, not presented here, is approximately $0.09U_b$. Values of $\langle v \rangle$ are typically below $0.05U_b$, indicating the mean flow profile is predominantly one-dimensional. At locations near the burner exit, profiles of $\langle v \rangle$ are relatively flat, whilst at further downstream locations, values of $\langle v \rangle$ increase slightly as the ambient is approached from the centre of the jet in the radial direction. The anisotropy in turbulence within the jet can be observed from comparing the fluctuating component of the axial and radial droplet velocities, u_{RMS} and v_{RMS}, respectively. Close to the burner exit (0.14D), values of u_{RMS} are approximately $0.9v_{RMS}$, and show a slight increasing trend in the radial direction of the jet to values of $1.0v_{RMS}$ at the boundary. With increasing distance downstream, v_{RMS} decreases faster than u_{RMS}. At a distance 4D downstream, values of u_{RMS} are approximately $1.1v_{RMS}$ near the centre of the jet, decreasing to $0.8v_{RMS}$ near the jet boundary.

The SMD values of the droplets in the non-reacting jet are predominantly in the 40–45 μm range, increasing slightly beyond this range near the jet boundary. The profiles show a small increase in the size of the droplets measured downstream, with some occasional variation in the droplet size present along the radial direction of the jet. Generally, we can observe from the droplet size and velocity measurements of the non-reacting jet a well defined, relatively uniform, turbulent droplet-air mixture, which is sufficient for the purposes of this study.

For the reacting cases, profiles of $\langle u \rangle$ take a top-hat shape near the exit, and subsequently flatten out within the combustion region with increasing distance downstream from the burner exit. In comparison to the non-reacting case, the presence of reaction is observed to sustain the axial velocity of the droplets in the downstream regions. For the axial location 4D from the burner exit, droplet size and velocity measurements were obtained in the radial direction only for $r/D \geq 0$ to avoid excessively long burner operation times. This is due to the low data rates, and consequently long signal acquisition times, at this axial distance. The radial profiles of $\langle u \rangle$ are observed to be more symmetric for low ϕ_{ov} conditions (ES1), and become more asymmetric with increasing Q_f (ES3). Values of $\langle u \rangle$ also increase with ϕ_{ov}, again showing the positive effect of heat release in sustaining the velocity of the droplets. Values of u_{RMS} are similar for all reacting cases, ranging from $0.175U_b$ near the burner exit and decreasing to approximately $0.1U_b$ downstream. Compared to the non-reacting case, radial profiles of u_{RMS} are flatter in the presence of heat release, and a similar

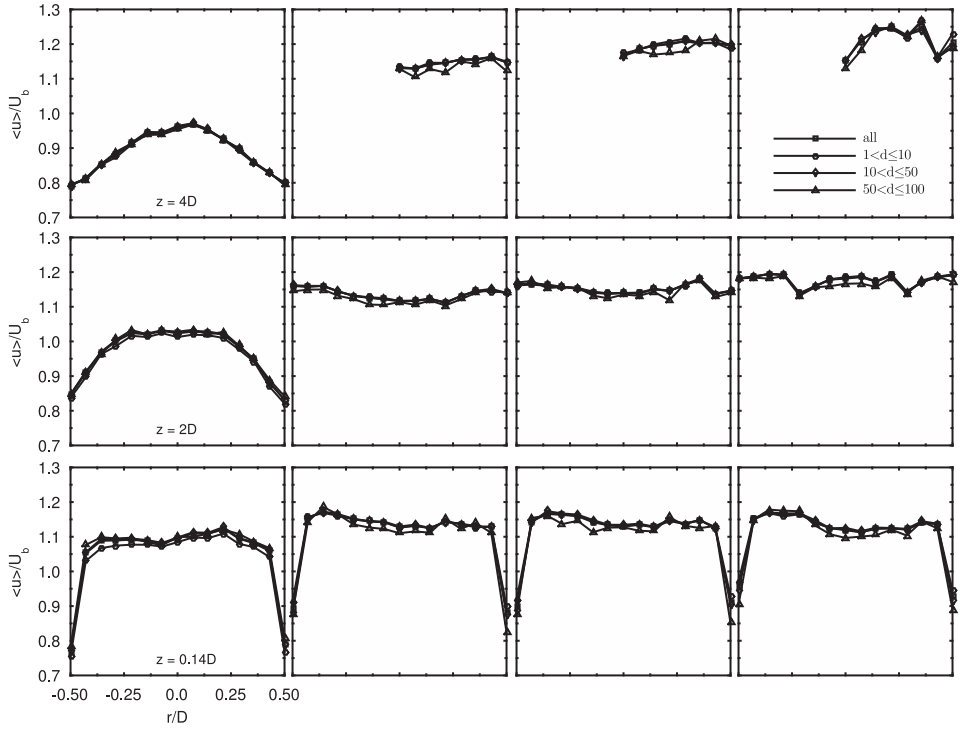

Fig. 6. Plots of $\langle u \rangle / U_b$ conditioned on three different droplet diameter classes ($1 < d[\mu m] \leq 10$, $10 < d[\mu m] \leq 50$, $50 < d[\mu m] \leq 100$) at axial locations from the burner exit of $0.14D$, $2D$ and $4D$ (rows bottom to top) for a non-reacting case (ES3 with pilot off) and for the spray flame at conditions ES1, ES2 and ES3 (columns left to right).

observation follows from the profiles of v_{RMS}. For the latter, values of v_{RMS} are observed to decrease with distance downstream, ranging from approximately $0.2U_b$ near the burner exit to approximately $0.07U_b$ downstream. This is a slightly wider range of v_{RMS} than that measured for the non-reacting case.

Greater anisotropy in the turbulence is observed in the presence of reaction. At condition ES1, values of u_{RMS} are again approximately $0.9v_{RMS}$ close to the burner exit ($0.14D$) at the centre of the jet. However, at a distance $4D$ downstream, values of u_{RMS} are approximately $1.4v_{RMS}$ at the centre of the jet. The anisotropy in the turbulence downstream increases with ϕ_{ov}. At condition ES3, values of u_{RMS} reach $1.7v_{RMS}$ at the centre of the jet. The trend of increasing u_{RMS}/v_{RMS} in the radial direction of the jet at axial locations close to the burner exit, which then reverses further downstream, observed for the non-reacting case is also observed under reacting conditions.

SMD values for the reacting cases are within the 30–43 μm, a decrease over the non-reacting case. However, similar trends in the SMD values along the axial and radial directions of the jet as for the non-reacting case are observed, with the increase in SMD with distance downstream more apparent. Additionally, the SMD values are also observed to increase with ϕ_{ov}, noting that only the fuel loading (Q_f) is increased while the atomizing air flow rate remains fixed.

Profiles of $\langle u \rangle$ and u_{RMS} conditioned on the droplet diameter (d) are shown in Figs. 6 and 7, respectively. In the figures, the velocity data is conditioned on three different droplet diameter classes: $1 < d[\mu m] \leq 10$, $10 < d[\mu m] \leq 50$ and $50 < d[\mu m] \leq 100$. The unconditioned velocity data is also shown in the plots for comparison purposes, with radial profiles of the conditioned velocity data plotted for axial locations of $0.14D$, $2D$ and $4D$. Profiles of $\langle u \rangle$ are discussed first. Considering droplet velocity measurements for the non-reacting case shown in Fig. 6, droplets in the smallest size class ($1 < d[\mu m] \leq 10$) are observed to have slightly smaller $\langle u \rangle$ values (by approximately $-0.014U_b$) than larger size droplets at locations close to the burner exit. This difference decreases with distance downstream, and eventually droplets of all size classes take on similar axial velocities. In contrast, for the reacting cases, droplets in the largest size class ($50 < d[\mu m] \leq 100$) generally have smaller $\langle u \rangle$ values than smaller size droplets, such as up to approximately $-0.017U_b$ at locations near the burner exit. Little difference is observed between the conditioned $\langle u \rangle$ profiles of the reacting cases with increasing ϕ_{ov}.

Analysing the conditioned u_{RMS} profiles in Fig. 7, droplets in the largest size class ($50 < d[\mu m] \leq 100$) generally have smaller u_{RMS} values than smaller sized droplets for both reacting and non-reacting cases. This is particularly evident at axial locations close to the burner exit, where differences of approximately $-0.015U_b$ are observed. For the non-reacting and the low ϕ_{ov} (ES1) cases, the difference in u_{RMS} values between the largest and smallest droplet size classes decreases to approximately $-0.005U_b$ downstream. For higher ϕ_{ov} conditions (ES2 and ES3), droplets in the largest size class can have lower u_{RMS} values than those in the smallest size class at the furthest downstream location investigated, decreasing to approximately $-0.03U_b$. At these downstream locations, larger differences in u_{RMS} values between droplets in the two smaller size classes are also observed compared to locations close to the burner exit. Studies in the literature have showed the magnitude of RMS velocity fluctuations of droplets in similar spray burner systems are smaller than those of the carrier air [33]. However, we may reasonably consider u_{RMS} values of the smallest droplets to closely approximate that of the carrier air, allowing an estimate of the flow turbulent Reynolds number ($Re_t = u'_{air} L_t/\nu$) to be obtained. At locations near the burner exit ($0.14D$), the smallest droplets within the jet have u_{RMS} values of $0.17U_b$, which we use as an estimate of u'_{air}. The integral length scale of the flow is approximated as $0.1D$ (4.2 mm). Neglecting evaporative cooling of the air inside the burner, we assume an air temperature of 286 K ($\nu = 1.45 \times 10^{-5}$ m^2/s) at the exit. This gives a Re_t value of 139, indicating a turbulent carrier air stream.

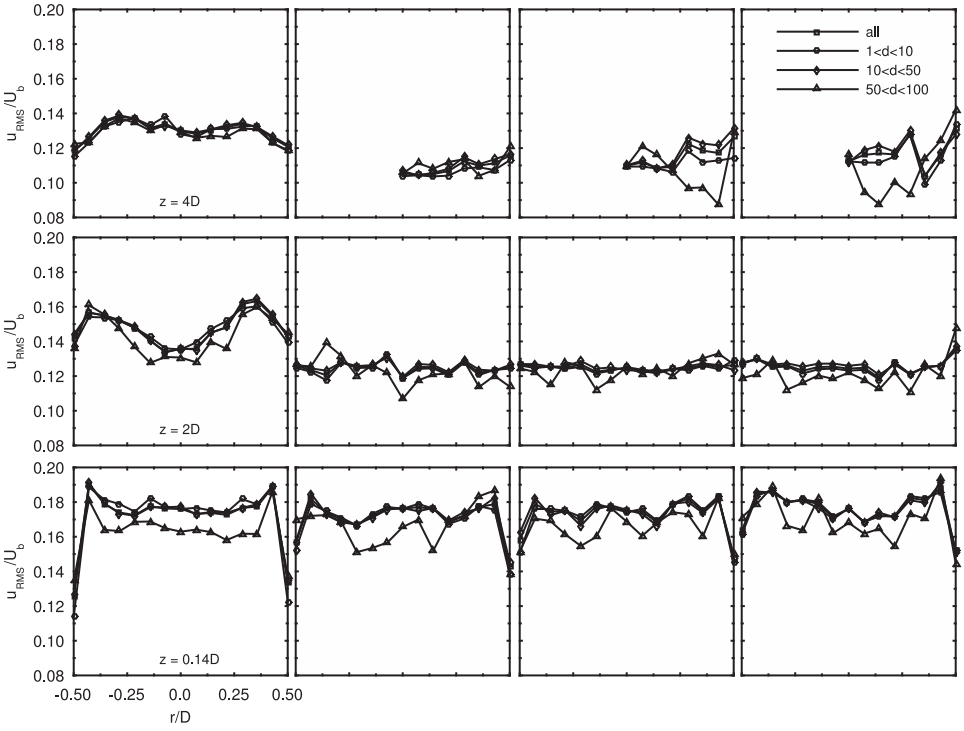

Fig. 7. Plots of u_{RMS}/U_b conditioned on three different droplet diameter classes ($1< d[\mu m]\leq 10$, $10< d[\mu m]\leq 50$, $50< d[\mu m]\leq 100$) at axial locations from the burner exit of 0.14*D*, 2*D* and 4*D* (rows bottom to top) for a non-reacting case (ES3 with pilot off) and for the spray flame at conditions ES1, ES2 and ES3 (columns left to right).

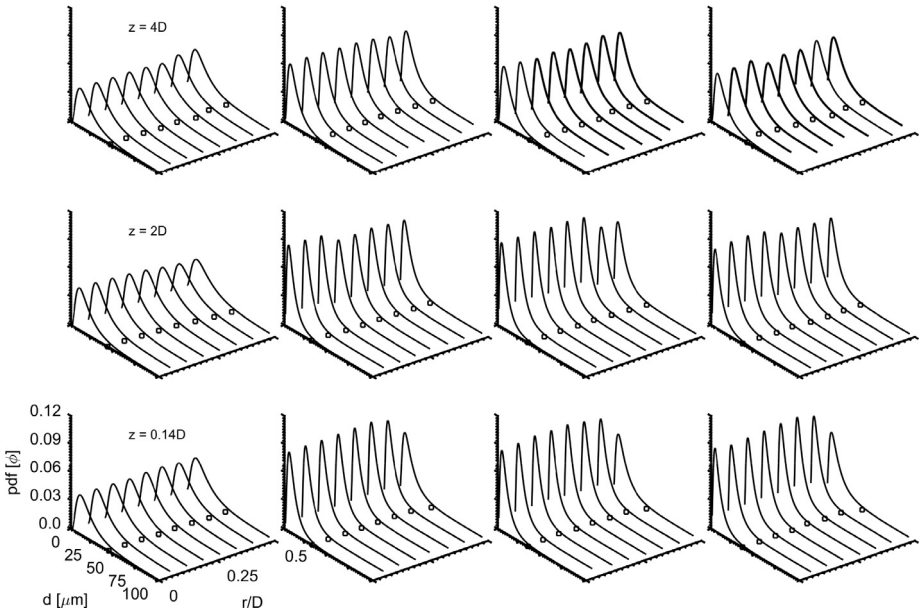

Fig. 8. Plots of the probability density function (*pdf*) of the droplet diameter for axial locations from the burner exit of 0.14*D*, 2*D* and 4*D* (rows bottom to top), for a non-reacting case (ES3 with pilot off) and for the spray flame at conditions ES1, ES2 and ES3 (columns left to right).

Distributions of the probability density function (*pdf*) of the droplet diameter for both the non-reacting and reacting cases are shown in Fig. 8. In each plot, a lognormal *pdf* is fitted to the normalized histogram of the droplet diameter values for each probe location along the radial direction of the jet. Droplet size *pdf* distributions are shown for three axial locations, 0.14*D*, 2*D* and 4*D*, and the square markers indicate the SMD value evaluated at each probe location. For the non-reacting case, the distributions of droplet diameter are generally similar along the radial direction of the jet. For axial locations of 0.14*D* and 2*D*, a slightly wider distribution of droplet diameter is observed near the edge of the jet. The SMD value at these axial locations follows a similar trend, increasing near the edge of the jet. For the reacting cases, the distributions near the edge of the jet at the axial location close to the burner exit (0.14*D*) are shorter and wider compared to the non-reacting case, with this behaviour also observed occasionally at further downstream locations. This behaviour may arise from faster evaporation of smaller droplets near the pilot flame, together with any accumulation of liquid fuel on the burner walls from droplet impacts which could lead to the shedding of larger droplets at the nozzle perimeter. Generally, the difference between the distributions along the radial direction decreases with distance

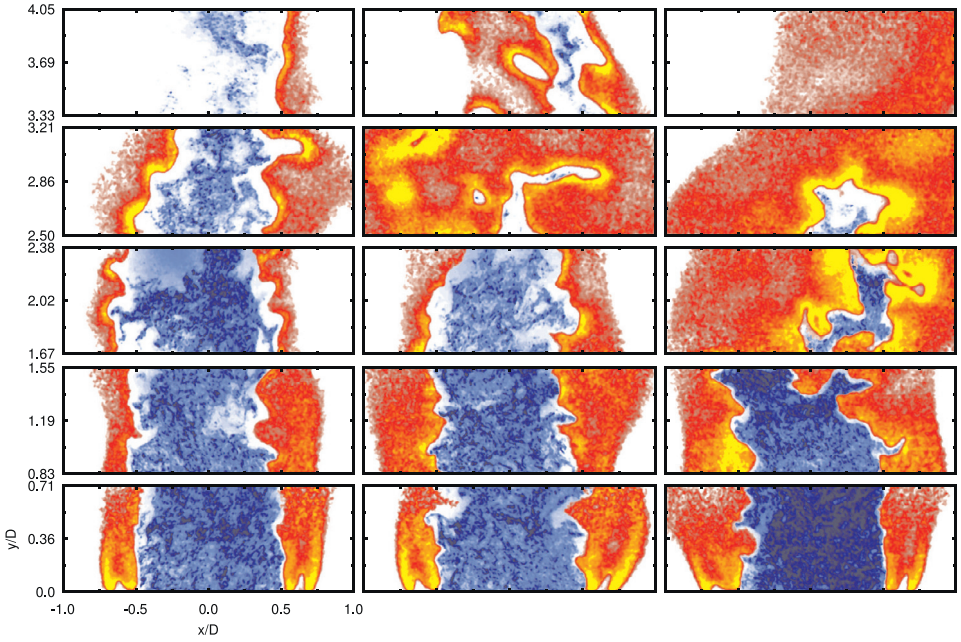

Fig. 9. Instantaneous images of simultaneously acquired OH PLIF and Mie scattering of the spray flame at conditions ES1, ES2 and ES3 (left to right). The red-to-yellow colour scale indicates increasing OH PLIF signal, and the light-to-dark blue colour scale indicates increasing Mie scattering of laser light off the fuel droplets. (For interpretation of the references to colour in this figure legend, the reader is referred to the web version of this article.)

downstream. Additionally, the distributions across the jet widen with distance downstream, with this trend becoming more significant both in the presence of reaction and with higher ϕ_{ov}. The changes in the distributions agree with the expected trend of increasing droplet evaporation in regions of higher mean temperatures, which follow the change of the mean flame shape from cylindrical to conical with increasing ϕ_{ov}, which is also observed in the trend of SMD values presented in Fig. 5.

3.3. Simultaneous OH PLIF and Mie scattering

Typical instantaneous images of the simultaneously acquired OH PLIF and Mie scattering signals are shown in Fig. 9. The height of the laser sheet used to induce fluorescence of OH restricts the imaging area of the simultaneously acquired signals to a height of 30 mm. Therefore, 5 regions separated axially are imaged at different time instances and plotted here in the same figure for convenience. For condition ES1, the OH PLIF signal shows the instantaneous flame shape to be cylindrical. The OH PLIF signal is present predominantly along the shear layer of the axisymmetric jet. The edge of the OH PLIF signal adjacent to the Mie signal tentatively marks the location of the instantaneous spray flame front. Strong OH emission is observed at both the location of the pilot flame and adjacent to the boundary of the droplet-laden mixture, and decreases as the ambient surrounding is approached in the radial direction. The Mie scattering signal shows fuel droplets survive at downstream locations extending to 4*D* from the burner exit. The visible decrease in the Mie signal intensity at axial locations 3–4*D* downstream indicates a lower droplet density than at regions further upstream, in qualitative agreement with the lower data rates observed for the PDA and LDA measurements at these downstream locations compared to axial locations close to the burner exit.

At condition ES2, the instantaneous flame takes a cone shape, closing across the jet at a downstream location of approximately 3*D*. The high intensity regions of OH remain predominantly adjacent to the edge of the jet, as observed for condition ES1. However, a wider distribution of low intensity OH is observed, particularly at the location where the instantaneous flame closes across the jet. The Mie signal shows the presence of droplets near the downstream location where the flame closes across the jet, with droplets also present at regions 4*D* downstream for instances when the instantaneous flame may not close across the flow. At condition ES3, the instantaneous flame is visibly shorter, taking a cone shape closing across the jet at an axial location approximately 3*D* downstream. High intensity OH is observed at this location, together with a wider spatial distribution of low intensity OH along the length of the flame. For this set of instantaneous images, the Mie signal is not present past regions 3*D* downstream, indicating that fewer droplets survive past the shorter flame at this condition.

The instantaneous images also show a region between the OH and Mie profiles void of any signal. Such regions are likely to contain a fuel vapour-air mixture at an insufficient temperature to generate OH. The width of this region is relatively small at axial locations close to the burner exit, and widens further downstream. At a given axial location, the width of this region appears to diminish as ϕ_{ov} is increased. We could expect a steeper temperature gradient between the reactant jet and flame front to result in a narrower fuel vapour-air region void of both droplets and production of OH. Such regions would exist at the jet boundary near the pilot flame and base of the spray flame, and adjacent to the spray flame front with increasing ϕ_{ov}. This would result in a flame front closer to the droplet-laden mixture at these regions and conditions compared to lower ϕ_{ov} conditions and regions away from the continuous pilot which possibly experience higher volumetric heat losses to the surrounding ambient.

Similar observations from these instantaneous images appear in the ensemble-averaged simultaneous OH PLIF and Mie scattering images shown in Fig. 10. At condition ES1, the average OH PLIF signal shows the average flame shape is cylindrical, with the average Mie signal showing fuel droplets survive at axial locations 4*D* downstream. As the liquid fuel flow rate (Q_f) is increased to condition ES2, the average flame shape is observed to change to a cone, with a visibly wider distribution of OH observed. The weaker intensity of the average Mie signal shows the presence of fuel droplets downstream decreases. These trends continue with higher

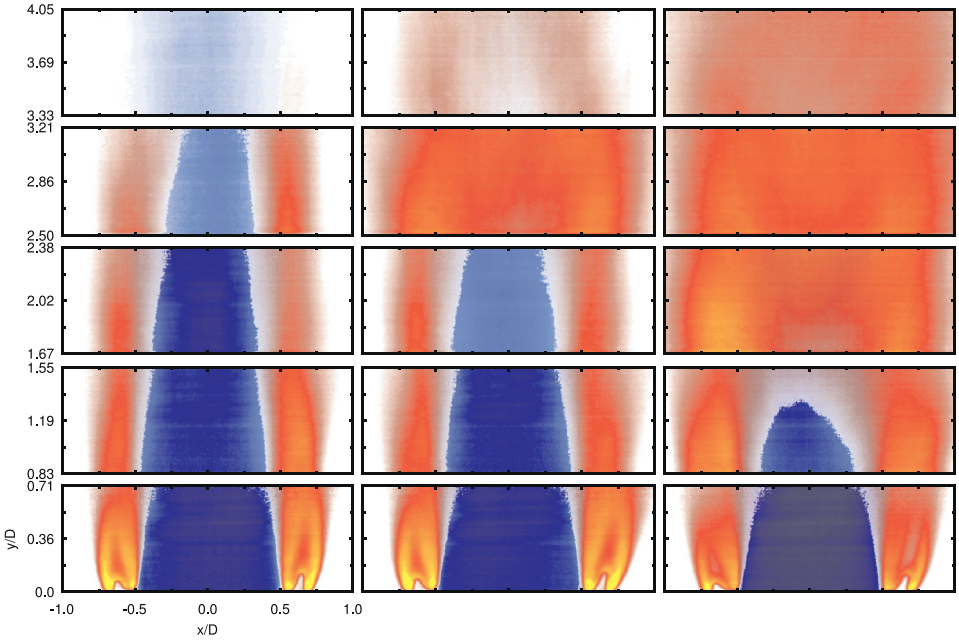

Fig. 10. Ensemble-averaged images of simultaneously acquired OH PLIF and Mie scattering of the spray flame at conditions ES1, ES2 and ES3 (left to right). The red-to-yellow colour scale indicates increasing OH PLIF signal, and the light-to-dark blue colour scale indicates increasing Mie scattering of laser light off the fuel droplets. (For interpretation of the references to colour in this figure legend, the reader is referred to the web version of this article.)

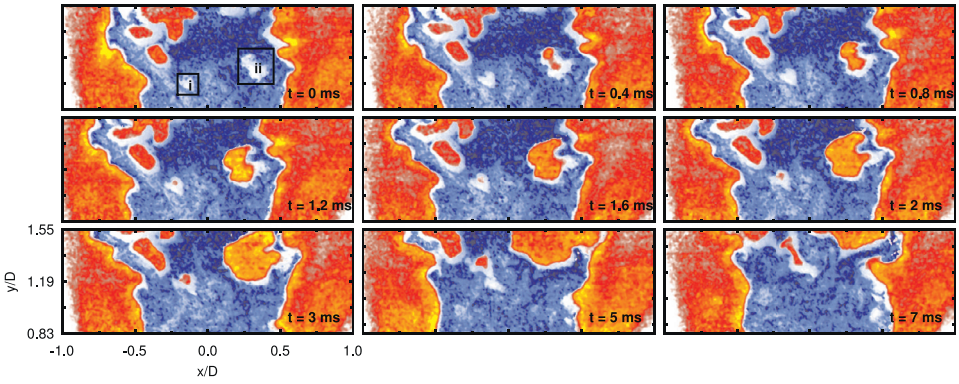

Fig. 11. Temporal sequence of instantaneous images of simultaneously acquired OH PLIF and Mie scattering of the spray flame at condition ES3 at the axial region of 0.83–1.55*D* from the burner exit. The red-to-yellow colour scale indicates increasing OH PLIF signal, and the light-to-dark blue colour scale indicates increasing Mie scattering of laser light off the fuel droplets. (For interpretation of the references to colour in this figure legend, the reader is referred to the web version of this article.)

Q_f at condition ES3, with the average flame brush closing across the flow further upstream (at a location of approximately 2*D*) than at condition ES2 (approximately 3*D*). The average flame shape from the OH PLIF signal also agrees with that from the OH* chemiluminescence signal and flame photographs presented earlier.

From observing the temporal behaviour of the instantaneous spray flame, as shown in Fig. 11, structures of OH appear within the jet at regions downstream from the burner exit, with their frequency of occurrence increasing with ϕ_{ov}. These structures either consist of low intensity OH, or can contain regions of high intensity OH, and consequently high OH gradients, indicating the presence of reaction. These OH structures typically appear in regions of low Mie signal intensity within the jet, and grow as they consume the local reactant mixture within their surrounding. These structures are then convected downstream with the main flow and eventually join the main flame located at the boundary of the jet. Examples of this behaviour are observed in Fig. 11, where at an arbitrary time (denoted as $t = 0$ ms) two regions of very low Mie intensity are identified by the two boxes labelled *i* and *ii* (image in top row of left column). After a short duration, OH structures are observed to originate from these regions (0.4 ms and 1.2 ms and for regions *i* and *ii*, respectively). As the centre of the jet is filled with cold reactants, their presence within the jet could arise from an out-of-plane connection with the main flame at the jet boundary. This indicates the behaviour of the flame at these downstream regions is more complicated than that at locations close to the burner exit where no significant evidence of out-of-plane motion of flame fronts is observed.

From the instantaneous images discussed above, it is not clear whether droplets penetrate the flame front. To investigate this, scatter plots of the instantaneous Mie scattering vs. OH PLIF signals were evaluated. Figure 12 shows arbitrary chosen scatter plots of these signals at the separately imaged regions of the flame, for the conditions investigated (ES1 to ES3). Before analysing the results, it is worth discussing the errors associated with overlapping the acquired OH PLIF and Mie scattering profiles. The OH PLIF laser sheet is approximately 0.25 mm thick, whilst the Mie scattering laser sheet is approximately 1 mm thick. Therefore, droplets adjacent to a structure of OH along the depth of field of the Mie scattering imaging system would be wrongly observed to overlap with

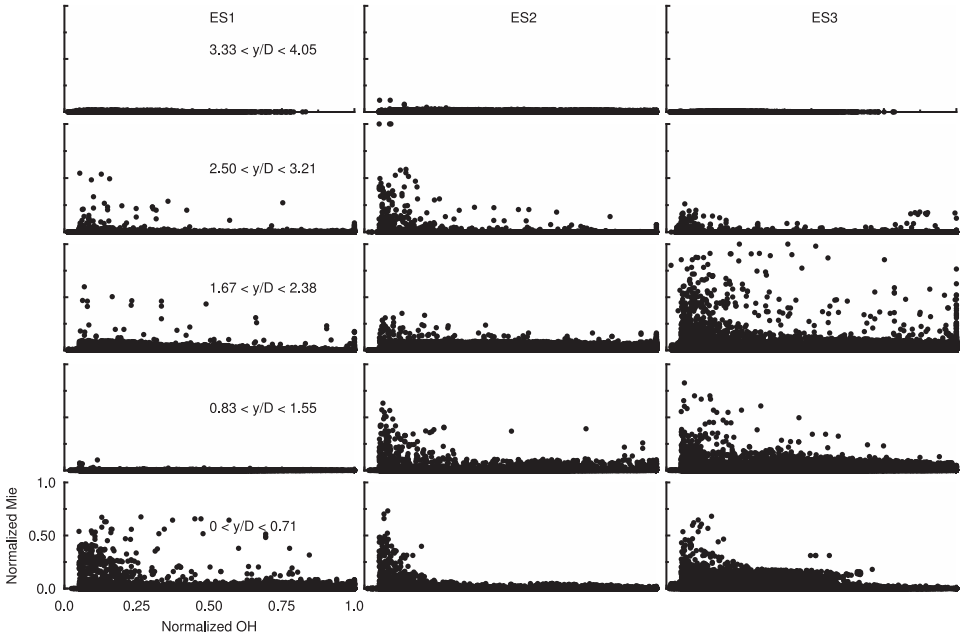

Fig. 12. Scatter plots of the normalized instantaneous Mie scattering vs. OH PLIF signals of the spray flame at conditions ES1, ES2 and ES3 (columns left to right) and the five separate imaged regions (y/D increasing bottom to top row).

the OH structure. Considering that droplets have an average diameter of approximately 30–50 μm, misalignments of the laser sheets within the estimated experimental uncertainty of 0.1 mm could be significant. This error is likely to manifest at the downstream locations where the flame front is more contorted and located closer to the centre of the jet, and may not be significant at locations near the burner exit where the flame front is relatively flat and located at the jet boundary.

The scatter plots in Fig. 12 show a general trend of decreasing Mie intensity with increasing OH intensity. High values of the Mie signal are typically observed to coincide with low-to-intermediate values of OH. Occasionally, low-to-intermediate values of Mie are observed at intermediate-to-high values of OH. However, this mostly occurs for regions downstream between $1.67D \leq y \leq 3.21D$ and for conditions ES2 and ES3, corresponding to the location where the flame closes across the jet. At these regions and conditions, significant differences in the scatter plots are observed over the image sets. Some of this variation may arise from the error associated with adjacent droplets appearing to overlap with OH regions described above. However, we can also expect greater droplet-flame interaction at locations where the flame brush closes across the jet, where droplets may possibly penetrate the initial spray flame front and continue to evaporate in regions of high OH intensity.

The droplet-flame interaction behaviour was also investigated by evaluating the pixel count of the binary Mie profile overlapping with the normalized OH profile. The results are reported using normalized histograms in Fig. 13. The results agree with the scatter plots of the instantaneous Mie vs. OH signals, with the Mie signal (and therefore droplets) predominantly occurring in regions of low OH. A visible decrease in the presence of droplets in low OH regions, which coincides with an increase in droplets in intermediate OH regions, appears for condition ES1 at the downstream region of $1.67D \leq y \leq 2.38D$. This is also observed for condition ES2. However, for condition ES2, this trend remains at further downstream regions, whilst disappearing for condition ES1. At condition ES3, a significant presence of droplets in intermediate OH regions is observed at axial locations closer to the burner exit, $0.83D \leq y \leq 1.55D$. At the downstream region $1.67D \leq y \leq 2.38D$, droplets appear present in high OH regions. Further downstream, the trend reverses and droplets primarily coincide with low-to-intermediate OH regions, with the shape of the histograms indicating a decrease in droplet density.

A further inspection of the flame-droplet interaction behaviour was performed by evaluating the average profiles of the instantaneous OH PLIF and Mie scattering signals in the direction normal to the flame front. For each image, the flame normal was evaluated at 10 evenly spaced points along each detected flame edge. Profiles of OH PLIF and Mie scattering along the directions pointing towards the burnt gas (increasing OH) and reactants (increasing Mie) regions were evaluated up to a distance of approximately 2 mm. These profiles were then averaged for each of the separately imaged regions for each flame condition (ES1 to ES3). When interpreting these results, errors previously discussed when presenting the Mie vs. OH scatter plots (Fig. 12) apply together with errors arising from matching the coordinate sets of the two cameras to obtain the overlapped image. The latter is estimated to be of the order of 1 pixel length, approximately 0.1 mm from the imaging resolution. Other errors also include post-processing of the raw OH PLIF and Mie scattering signals, from which a sensitivity analysis of the chosen signal filtering and threshold values were determined not to be significant. The averaged profiles are shown in Fig. 14, where L_N denotes the distance from the flame front (located at the origin, $L_N = 0$) along the flame normal, with positive (negative) L_N values denoting the burnt gas (reactants) region of the flame.

The OH and Mie signals for all imaging regions and flame conditions investigated were normalized by the same maximum OH and Mie intensity values to compare trends across the imaging regions and flame conditions. As expected, the Mie profiles show a decreasing trend in the direction normal to the flame front as approached from the reactant side, with relatively low Mie signals ($< 5\%$ intensity) evaluated on the burnt gas side of the flame front for condition ES1. For higher fuel loading (Q_f), the Mie intensity approaching the flame front from the reactants side expectedly increases. A small, but visible, increase in Mie intensity in the burned gas region is also observed with increasing Q_f, possibly indicating an increase in droplets penetrating the flame front. The profiles also show a general trend of decreasing Mie intensity local to the

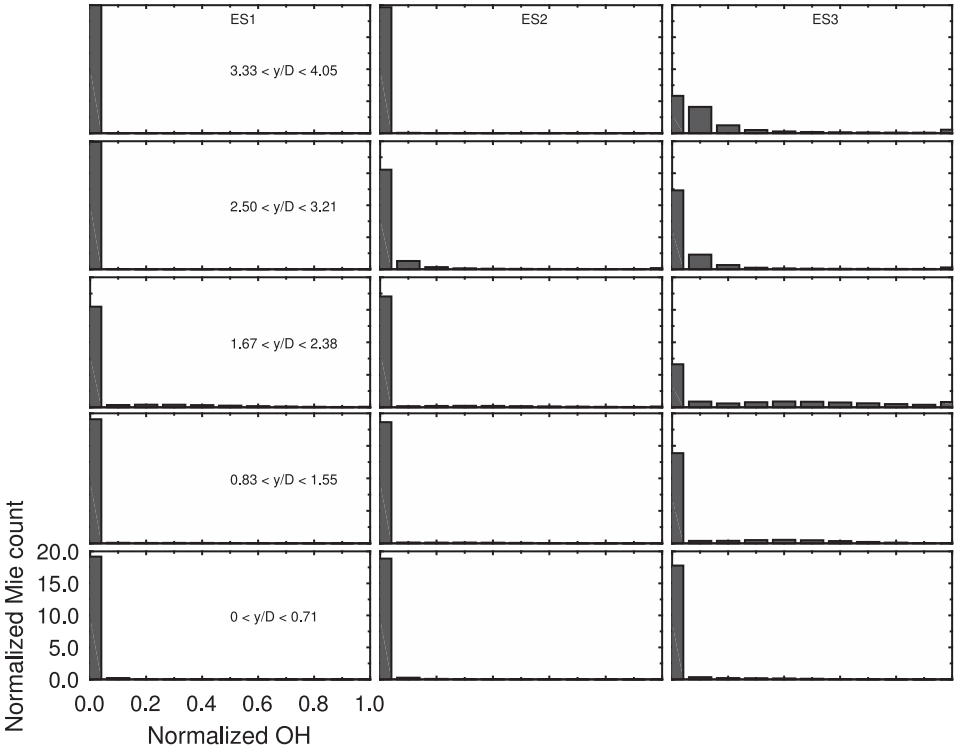

Fig. 13. Normalized histograms of the pixel count of the overlapping normalized OH PLIF and Mie scattering signals of the spray flame at conditions ES1, ES2 and ES3 (columns left to right) and the five separate imaged regions (y/D increasing bottom to top row).

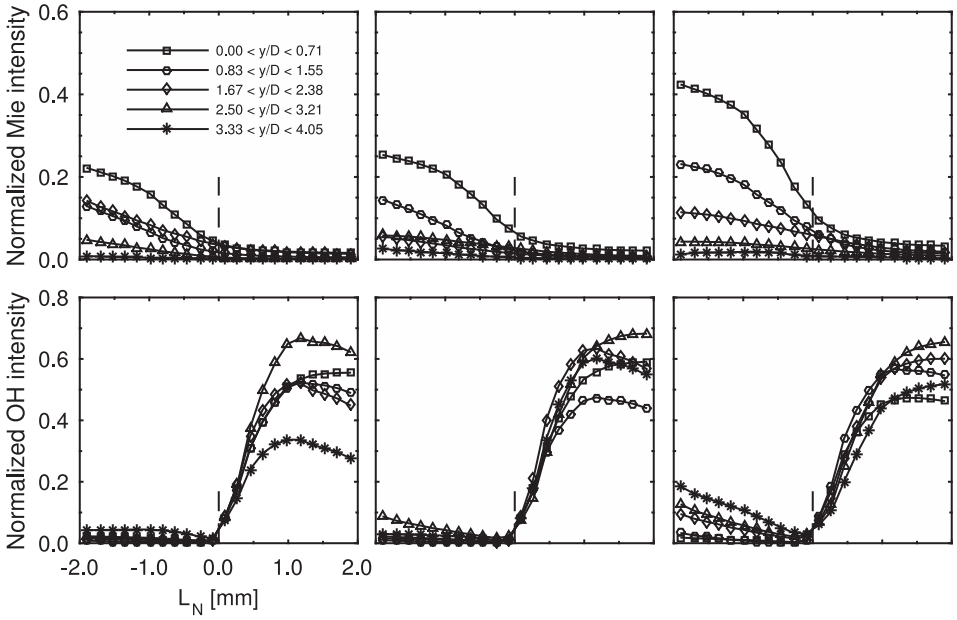

Fig. 14. Plots of the averaged profiles of the instantaneous normalized intensity of the OH PLIF (bottom row) and Mie scattering (top row) signals in the direction normal to the instantaneous flame front of the spray flame at conditions ES1, ES2 and ES3 (left to right). $L_N = 0$ indicates the instantaneous flame front location, with $L_N > 0$ (< 0) indicating the burnt gas (reactants) side of the flame front.

flame front with increasing distance downstream from the burner exit. This would agree with an expected decrease in droplet density with distance downstream along the flame brush.

The OH profiles, in general, show the expected trend of low OH on the reactant side, increasing across the flame front to attain a maximum value on the burnt gas side. However, a trend of increasing OH on the reactants side appears at condition ES2 at locations near where the flame closes across the jet, and becomes more significant at condition ES3 at these and further downstream regions. This may result from an increased presence of OH structures closely located to the flame front on the reactants side, and from a more contorted flame front. No clear trend of the OH signal intensity on the burnt gas side with either distance downstream from the burner exit, or with higher Q_f is observed. This may result from changes in the OH laser beam power between imaging sets not accounted for when applying a fixed value to

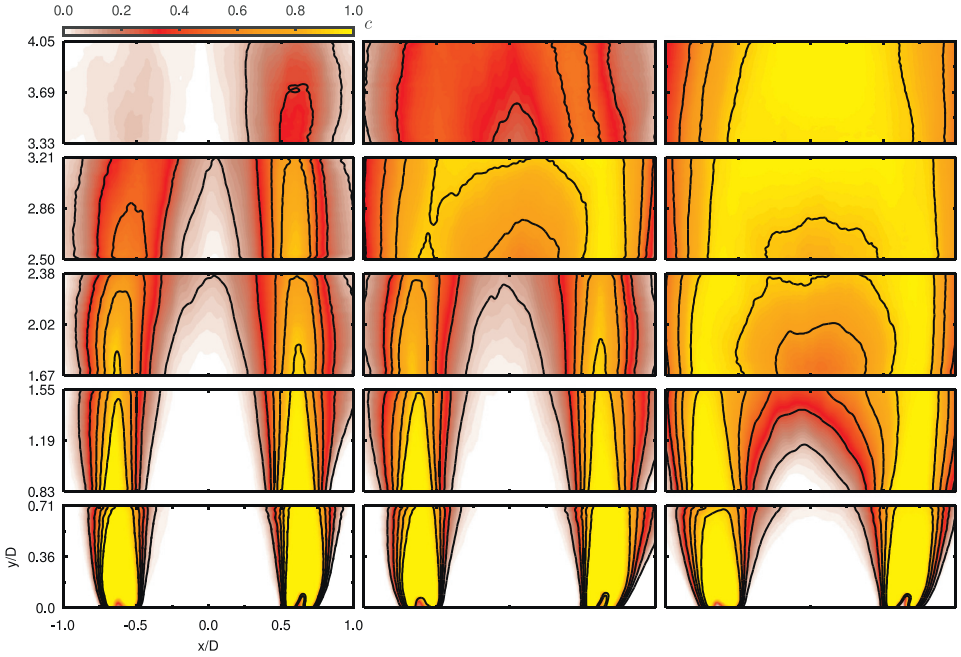

Fig. 15. Images of the ensemble-averaged reaction progress variable map $\langle c \rangle$ for conditions ES1, ES2 and ES3 (left to right).

normalize the OH PLIF data presented. From these profiles, droplet penetration appears significant at the downstream regions where the flame closes across the jet, with the average droplet penetration into the burned gas region less than 2 mm.

3.3.1. Reaction progress variable

Profiles of the ensemble-average reaction progress variable ($\langle c \rangle$) obtained from the OH PLIF images evaluated for conditions ES1 to ES3 are shown in Fig. 15. In the images, isocontours of $\langle c \rangle$ = 0.1, 0.3, 0.5, 0.7 and 0.9 are denoted by the black lines. At locations close to the burner exit, the $\langle c \rangle$ isocontours are closely spaced. At the downstream locations, the distance between the $\langle c \rangle$ isocontours increases, indicating a thicker mean flame brush. The discrepancy of the $\langle c \rangle$ contours between the separately imaged regions of the flame zone may result from changes in the mean flame shape and OH laser beam power between imaging sets. However, the key changes in the mean flame shape observed from the ensemble-average OH PLIF and OH* chemiluminescence images, and flame photographs, are again evident from the $\langle c \rangle$ isocontours. The shape of the mean flame brush at condition ES1 again appears cylindrical, and takes a cone shape at conditions ES2 and ES3. The length of the flame brush initially increases between conditions ES1 and ES2, with the length of the cone shaped flame decreasing at condition ES3. At locations close to the vertex of the cone shaped flame at conditions ES2 and ES3, the spatial distribution of burned gas identified by the high $\langle c \rangle$ values also agree with the PLIF images showing wide regions of low intensity OH.

3.3.2. 2-D flame surface density

Figure 16 shows measurements of the 2-D flame surface density (Σ) using the methods of Deschamps et al. [28] (top row, denoted as $\Sigma_{\nabla\langle c \rangle}$) and Shepherd [26] (bottom row, denoted as $\Sigma_{L/A}$) for the flame at conditions ES1 to ES3 at each of the five separately imaged regions shown in the OH PLIF images. Both methods are observed to give similar trends in Σ for the conditions investigated, and the profiles show a change in the flame structure with both distance downstream from the burner exit and increasing ϕ_{ov}. Considering condition ES1, at locations near the burner exit, the Σ profiles are similar to those obtained for fully premixed flames [27], with $\Sigma_{L/A}$ and $\Sigma_{\nabla\langle c \rangle}$ increasing for values of $\langle c \rangle$ approaching 0.5. This trend may be influenced by the premixed pilot flame at the burner exit. With increasing distance downstream, the profiles then flatten out and tend to zero, indicating a loss in flame surface. At the furthest downstream region imaged, the profiles are non-zero for $\langle c \rangle < 0.4$. This indicates that a stable flame is not established at this downstream region for this very lean condition, in agreement with the low emission observed in the mean flame images at this region.

At higher ϕ_{ov} conditions, both $\Sigma_{L/A}$ and $\Sigma_{\nabla\langle c \rangle}$ profiles close to the burner exit resemble those for condition ES1, with a slight decrease in their peak Σ value observed with increasing fuel loading. As for condition ES1, the profiles show a decreasing trend with distance downstream. The profiles also approach zero at regions closer to the burner exit, particularly for condition ES3, indicating in a loss in flame surface downstream. This would agree with a decrease in the flame length from conditions ES2 to ES3, as observed in the flame images presented earlier. The $\Sigma_{L/A}$ and $\Sigma_{\nabla\langle c \rangle}$ profiles also show a shift to higher $\langle c \rangle$ values at some downstream regions, which is also observed at condition ES1, possibly indicating reaction is increasingly occurring in regions predominantly occupied with burned gases.

3.3.3. 2-D flame front curvature

Plots of the probability density function (*pdf*) of the nondimensional curvature ($\kappa\delta_L$, δ_L is the laminar flame thickness for a premixed ethanol vapour-air mixture at phi_{ov} conditions) of the instantaneous flame front defined as the boundary between reactants (Mie scattering signal) and products (OH PLIF signal) from the simultaneous measurements reported earlier are shown in Fig. 17. Values of δ_L are provided in Table 1. At condition ES1, the distributions of $\kappa\delta_L$ are observed to be approximately Gaussian and symmetric about $\kappa\delta_L = 0$, with little change observed in the distributions with distance downstream from the burner exit. As ϕ_{ov} is increased to condition ES2, the distributions widen, indicating an increasing probability of obtaining higher magnitudes of flame front curvature. The distributions also widen slightly with distance downstream, further indicating a more contorted flame away from the burner exit. At condition ES3, the distributions are wider, with

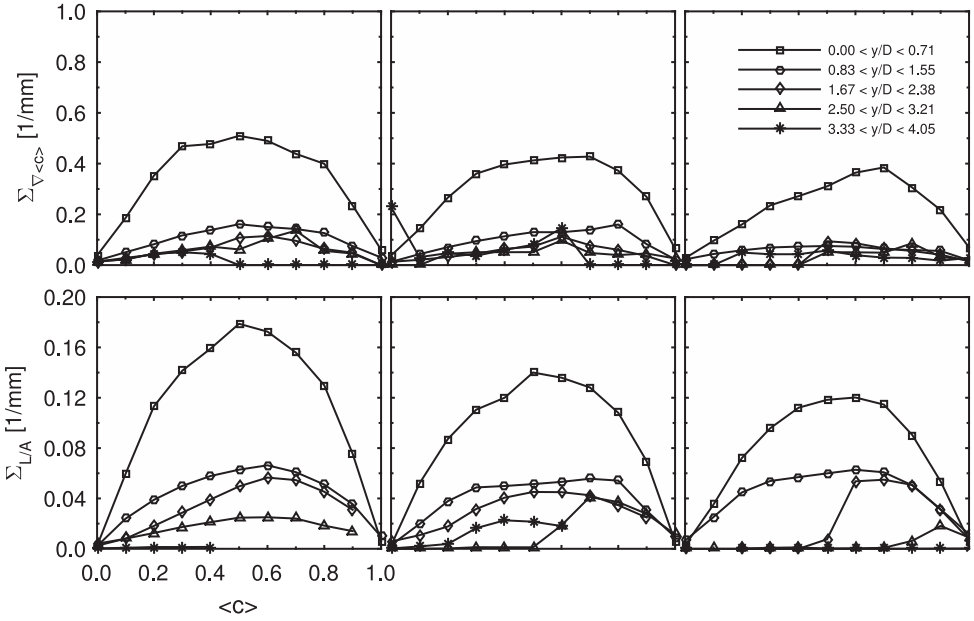

Fig. 16. 2-D estimates of the flame surface density using the methods of [26] (bottom row, $\Sigma_{L/A}$) and [28] (top row, $\Sigma_{\nabla\langle c\rangle}$) for the spray flame at conditions ES1, ES2 and ES3 (left to right) based on the OH signal.

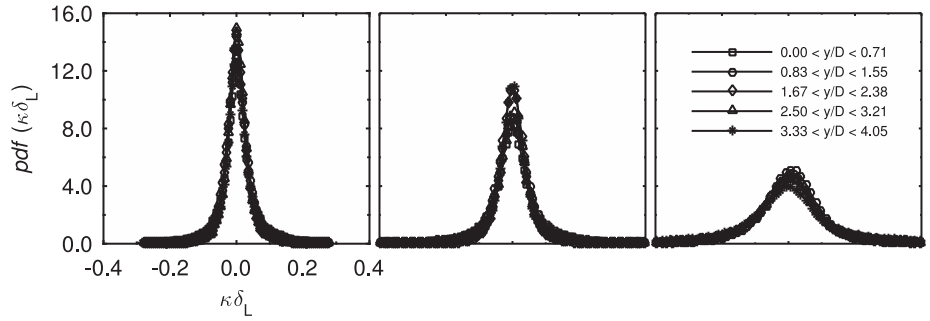

Fig. 17. 2-D estimates of the nondimensional flame front curvature ($\kappa\delta_L$) for the spray flame at conditions ES1, ES2 and ES3 (left to right) based on the OH signal.

a slight shift to positive curvature values observed. This may agree with the increased presence of isolated OH structures near the downstream location where the flame closes across the jet. These OH structures generally appear circular in shape, and likely to have a flame front with predominantly positive curvature values. These distributions are also in agreement with the flame imaging results which showed a more contorted instantaneous flame edge with both distance downstream and for higher fuel loading conditions (Fig. 9).

3.4. CH_2O-fuel PLIF

Instantaneous images of the CH_2O-fuel PLIF signal for the spray flame at conditions ES1 to ES3 are shown in Fig. 18. Calculations of laminar non-premixed gaseous ethanol-air flames performed by Yuan [34] showed CH_2O to be produced in the fuel rich side of the flame where it attains a maximum value. The CH_2O profile then decreases gradually as the stoichiometric mixture fraction value is approached, and a smaller local peak is attained prior to the complete consumption of CH_2O at the high reaction rate regions of the flame. The CH_2O and fuel profiles coincide in mixture fraction space, and both are consumed at the location of stoichiometric mixture fraction. As we don't observe droplets to burn in individual or group diffusion flame envelopes, a similar trend can also be expected for the ethanol spray flame investigated here. Therefore, we can tentatively consider the edge of the CH_2O-fuel PLIF signal to mark the high reaction rate region of the flame where both CH_2O and fuel are consumed, approximating the location of the local flame front.

This boundary is observed to be smooth and flat near the burner exit, and becomes more contorted with distance downstream for the conditions investigated. The highest CH_2O-fuel PLIF intensity regions are typically observed near the centre of the jet, with fuel fluorescence likely dominating the signal as CH_2O is unlikely to be significant near the centre of the cold jet of reactants. Relatively low CH_2O-fuel PLIF intensity regions are observed near the boundary of the jet, where a greater part of the signal is likely to be fluorescence of CH_2O following its production in higher temperature regions closer to the flame front. Occasionally, regions void of CH_2O-fuel PLIF appear within the jet. From the simultaneous OH PLIF and Mie scattering measurements, structures of OH were observed in regions within the jet and were suggested to result from out-of-plane motion of established flame fronts. We could therefore expect some of these regions within the jet void of CH_2O-fuel PLIF to have undergone reaction and contain burned gases following the rapid consumption of CH_2O and fuel in regions of high reaction.

The instantaneous CH_2O-fuel PLIF signal shown in Fig. 18 is also observed to have a grainy appearance. This is particularly evident at regions near the burner exit and close to the centre of the jet, where the CH_2O-fuel PLIF signal bears some resemblance to the Mie scattering signal. Collection of laser light scattering off the fuel

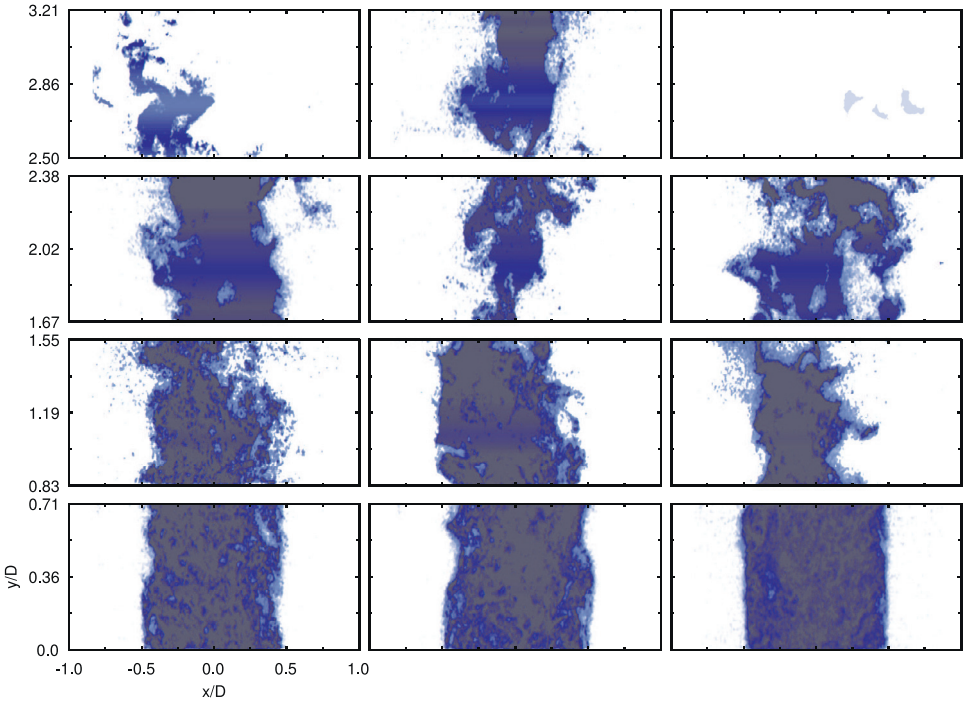

Fig. 18. Instantaneous images of CH_2O-fuel PLIF of the spray flame at conditions ES1, ES2 and ES3 (left to right). Light-to-dark blue colour scale indicates increasing CH_2O-fuel PLIF signal.

droplets by the imaging system is unlikely as a 355 nm notch filter was attached to the camera lens to prevent this. The grainy signal may then result from fluorescence of the fuel droplets interspersed within the CH_2O signal, which the imaging system could capture given the average inter-droplet diameter within the jet is greater than the pixel resolution of the measurements. Considering condition ES3 with volumetric fuel and air flow rates of $5.4\text{x}10^{-7}$ m^3/s and 3.9×10^{-3} m^3/s, respectively, and an average droplet diameter of 40 μm from the SMD results, the droplet number density per unit volume (n) evaluates to 4.1×10^9 *number of droplets*/m^3. For a dilute spray, the average inter-droplet distance can be approximated as $n^{-1/3}$ [8], evaluating to 620 μm. This value is approximately 5 times the pixel resolution (116 μm per pixel) and 15 times the assumed average droplet diameter (40 μm) which is in agreement with the dilute spray assumption. This indicates the acquisition system could capture fluorescence of individual ethanol droplets, resulting in the grainy appearance of the instantaneous CH_2O-fuel PLIF signal.

Images of the ensemble-averaged CH_2O-fuel PLIF signal superposed with isocontours of $\langle c\rangle = 0.1, 0.3, 0.5, 0.7$ and 0.9 (obtained from the binary OH PLIF signal presented earlier) denoted by the thick black lines are shown in Fig. 19. The time-averaged CH_2O-fuel PLIF signal is observed to extend to regions $3D$ downstream from the burner exit for the conditions investigated, with a general trend of decreasing intensity with distance downstream. The average CH_2O-fuel PLIF signal is observed in regions of low $\langle c\rangle$ values at axial locations near the burner exit. With increasing distance from the burner exit, an increasing amount CH_2O-fuel PLIF appears at intermediate-to-high $\langle c\rangle$ values, particularly for conditions ES2 and ES3. For condition ES3 at the axial location $1.67D \leq y \leq 2.38D$, the CH_2O-fuel PLIF signal is observed in regions typically occupied with high $\langle c\rangle$ values. This behaviour is also observed at the furthest imaged axial region of the flame for conditions ES1 and ES3. However, the average signals do not indicate the instantaneous CH_2O-fuel signal coincides with high reaction rate regions, and possibly hot products, for the conditions investigated.

The variation of the instantaneous CH_2O-fuel PLIF with the ensemble-averaged OH PLIF signal ($\langle OH\rangle$) was investigated by evaluating the pixel count of the binary CH_2O-fuel PLIF profile overlapping with the time averaged OH PLIF signal. The results are reported using normalized histograms in Fig. 20. At locations close to the burner exit, the CH_2O-fuel PLIF signal is observed in regions of low $\langle OH\rangle$ values. With increasing distance from the burner exit, an increasing amount of the CH_2O-fuel PLIF signal appears in regions of intermediate $\langle OH\rangle$ values. This is particularly evident for condition ES3 at the axial location $1.67D \leq y \leq 2.38D$, and for the furthest imaged axial region for conditions ES2 and ES3. This may be in agreement with observations of the instantaneous OH and Mie signals in Fig. 13 which showed the possible overlap of reactants with intermediate OH values at these regions. However, Fig. 20 shows no significant presence of the CH_2O-fuel PLIF signal in regions of high $\langle OH\rangle$ values. This would indicate little overlap of fuel droplets and vapour in regions of high OH, as observed from analysis of the simultaneous OH PLIF and Mie scattering data.

3.4.1. 2-D flame surface density

Considering the edge of the CH_2O-fuel PLIF signal to mark the local flame front, alternative estimates of the 2-D Σ and κ were evaluated. For the 2-D Σ estimates, the flame front detected from the CH_2O-fuel PLIF profile is superposed onto the $\langle c\rangle$ map obtained from the OH PLIF measurements. Estimates of $\Sigma_{\nabla\langle c\rangle}$ and $\Sigma_{L/A}$, Eqs. (1) and (2), respectively, are evaluated based on the CH_2O-fuel PLIF derived flame edge and are presented in Fig. 21. The trends generally agree with those evaluated based on the OH PLIF data shown in Fig. 16. At locations close to the exit, the highest Σ values are observed for $\langle c\rangle$ values near 0.5, again resembling fully premixed flames. Values of Σ then decrease with distance downstream, with the highest Σ values occurring at higher $\langle c\rangle$ values. This again indicates a shift of reaction to regions predominantly filled with burned gases, as observed from the OH PLIF based Σ data. However, the trend of decreasing Σ with higher ϕ_{ov} observed from the OH PLIF based data is not clear from the CH_2O-fuel PLIF, failing to

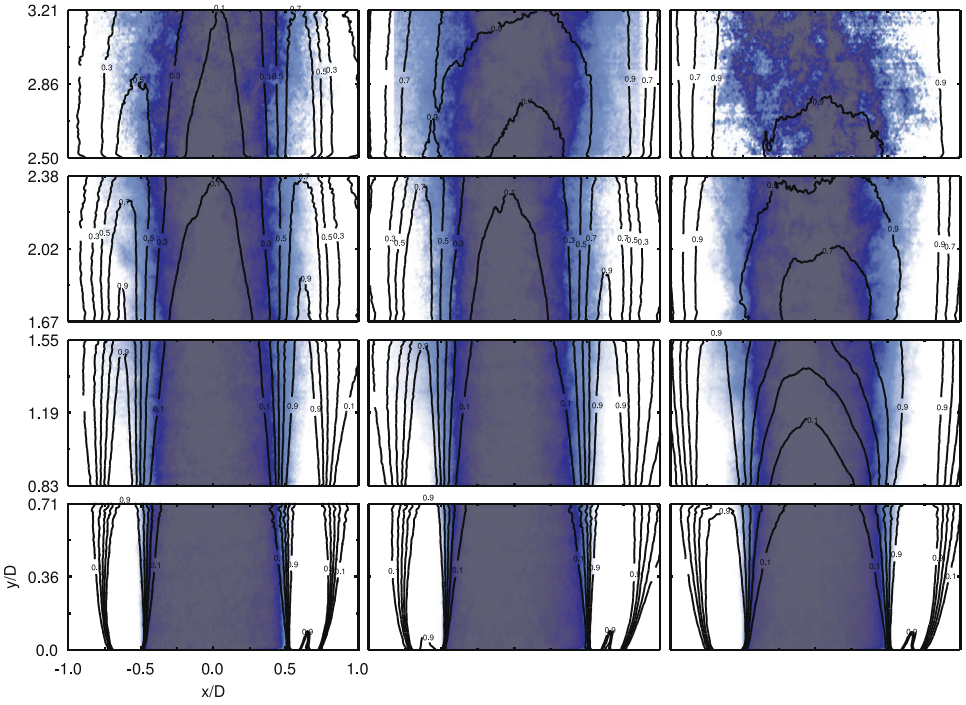

Fig. 19. Images of the ensemble-average CH_2O-fuel PLIF superposed with isocontours of $\langle c \rangle$ = 0.1, 0.3, 0.5, 0.7 and 0.9 (in the thick black lines) obtained from the OH PLIF data, of the spray flame at conditions ES1, ES2 and ES3 (left to right). Light-to-dark blue colour scale indicates increasing CH_2O-fuel PLIF signal.

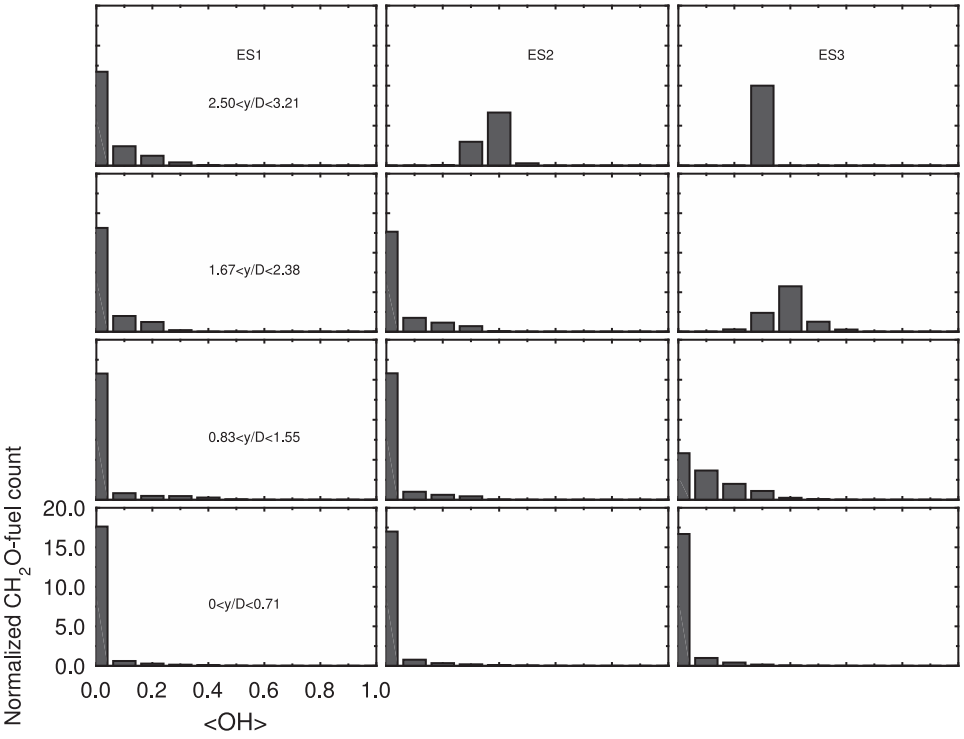

Fig. 20. Plots of the probability of occurrence of CH_2O-fuel PLIF signal within the time-averaged OH PLIF map for conditions ES1, ES2 and ES3 (left to right).

capture the increase in flame loss downstream as the flame height decreases. Additionally, the trends of Σ based on the CH_2O-fuel PLIF signal are not as clear as those based on the OH PLIF signal. Small variations in the chosen threshold value for the CH_2O-fuel PLIF profile result in visible changes in the Σ profiles not observed for the OH PLIF based Σ data. This may again result from the smaller sampling of the CH_2O-fuel PLIF measurements (200 images per recording set) compared to the OH PLIF measurements (5000 images per recording set), resulting in higher standard errors of approximately 5%.

3.4.2. 2-D flame front curvature

Distributions of the nondimensional 2-D flame front curvature ($\kappa \delta_L$) estimates based on the CH_2O-fuel PLIF profile are shown in Fig. 22. The distributions are similar to those of $\kappa \delta_L$ based on the OH PLIF signal, Fig. 17, taking a Gaussian shape symmetric about

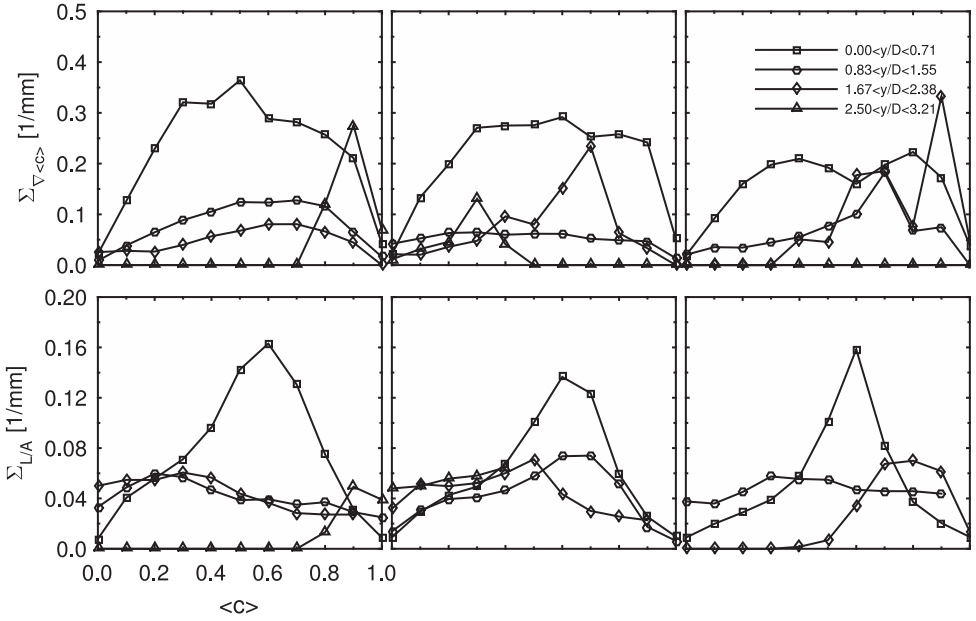

Fig. 21. 2-D estimates of the flame surface density using the methods of [26] (bottom row) and [28] (top row) for the spray flame at conditions ES1, ES2 and ES3 (left to right) based on the CH_2O-fuel PLIF signal.

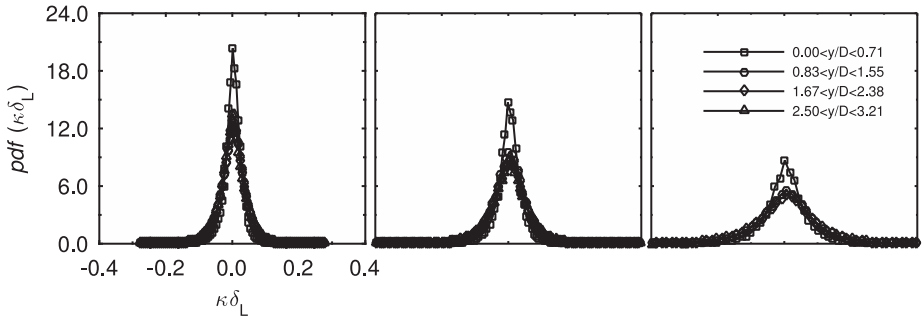

Fig. 22. 2-D estimates of the nondimensional flame front curvature ($\kappa\delta_L$) for the spray flame at conditions ES1, ES2 and ES3 (left to right) based on the CH_2O-fuel PLIF signal.

$\kappa\delta_L = 0$, and widening with both increasing distance downstream and with higher ϕ_{ov}. A noticeable difference is observed between the curvature distributions close to the burner exit and those further downstream, indicating larger changes in the degree of wrinkling of the CH_2O-fuel PLIF profile with distance downstream than the OH PLIF profile. However, the standard error of the curvature measurements based on the CH_2O-fuel PLIF profile is approximately 10%, double that for the curvature estimates based on the OH PLIF profile, and may therefore be less reliable.

4. Discussion and further processing

4.1. Droplet velocity and diameter

The general trends of the droplet size and velocity presented in this work agree with those reported in the literature for dilute sprays in simple, well defined flows where droplets of diameter less than 10 μm have been shown to have similar velocities to the carrier flow [24]. Assuming this holds for the present work, the results in Fig. 6 would indicate a general trend of larger droplets having negative axial slip velocities for reacting conditions. This was observed in [24] for both reacting and non-reacting conditions, and attributed to their higher inertia. However, for the non-reacting case at locations near the burner exit, Fig. 6 shows larger droplets to have higher axial velocities compared to smaller droplets, and therefore possibly positive slip velocities. This may result from deceleration of the carrier air expanding into the ambient, which is likely to have a delayed influence on larger droplets due to their higher inertia compared to smaller droplets. Eventually, droplets across the three size classes investigated are observed to have similar axial velocities at locations 4*D* downstream from the burner exit. The trend of higher magnitudes of slip velocity for larger droplets across the measured jet locations for the reacting cases in Fig. 6 compared to the non-reacting case also agrees with observations reported in [24].

The results in Fig. 7 indicate larger droplets have smaller axial velocity fluctuations than smaller droplets near the centre of the jet, with this difference deceasing near the edge of the jet. This trend was also observed in [10], and attributed to droplet interactions with the boundary layer developing from the inner wall of the burner. The general trends of the droplet size distributions presented in Fig. 8 are also in agreement with those reported in [10]. This includes trends of fewer droplets near the edge of the jet and a shift to larger droplet diameters with distance downstream, suggested to result from faster evaporation of both droplets near the flame at the jet boundary and smaller droplets within the jet with distance downstream along the flame zone.

The interaction of droplets with the carrier air turbulence can also be investigated through their average Stokes number (*St*). Following [35], $St = \tau_d/\tau_t$, where $\tau_d = (4d\rho_L)/(3C_D\rho_G\langle|u_G - u_L|\rangle)$ is

the droplet relaxation time, and $\tau_t = L_{1/2}/u_{G,\,RMS}$ is the turbulent time scale. Subscripts L and G are used to refer to liquid and gas phase properties, respectively. The standard deviation of the fluctuating gas phase velocity ($u_{G,\,RMS}$) is here approximated using the fluctuating velocity of droplets in the size class $1< d[\mu m]\leq 10$. Consequently, estimates of St are evaluated for droplets in two size classes, $10< d[\mu m]\leq 50$ and $50< d[\mu m]\leq 100$. $L_{1/2}$ is a large eddy length scale, here estimated as the half width of the jet at the burner exit ($D/2$) and assumed constant for all downstream locations investigated. Defining the Reynolds number of the droplets $Re_d = d\langle|u_G - u_L|\rangle/\nu_G$, the drag coefficient C_D=24(1+0.15$Re_d^{0.687}$)/Re_d. Estimates of St were evaluated along the centreline of the jet for both reacting and non-reacting conditions.

Droplets in the size classes $10< d[\mu m]\leq 50$ and $50< d[\mu m]\leq 100$ were estimated to have St values of approximately 0.009–0.015 and 0.07–0.13, respectively. Estimates of St generally decreased with distance downstream, except for droplets in the size class $10< d[\mu m]\leq 50$ at Z=4D, where a small increase was observed. Estimates of St are also larger for the non-reacting case compared to reacting conditions. As expected, these trends generally show the droplets to more closely follow the turbulent fluctuations of the carrier air both in the presence of reaction and with increasing distance downstream, with the exception of droplets in the size class $10< d[\mu m]\leq 50$ at the furthest downstream location measured. Considering the small values of the St estimates together with the expectation of larger droplets surviving further downstream, droplets in the downstream regions are suggested to closely follow the turbulent carrier air fluctuations than to group together. The appearance of groups of droplets at the downstream regions in Fig. 18 may arise from pockets of droplets penetrating the reaction sheet, perhaps in regions where the local equivalence ratio temporarily falls below the lean flammability limit causing local extinction, after which they continue to evaporate in the flow of unburned reactants and hot combustion products.

4.2. Droplet-flame interaction

The imaging studies of the average flame shape further support the general trends in the droplet size distributions. The average flame shape was observed to change from cylindrical to a cone-shape, initially increasing in length before decreasing as ϕ_{ov} is increased from conditions ES1 to ES3, Figs. 3 and 4. Together with the observed increase in average luminosity of the flame with ϕ_{ov}, and therefore heat-release, these changes indicate higher mean temperatures closer to both the centre of the jet and upstream towards the burner exit. This would lead to higher average droplet evaporation rates, causing both the droplets near the flame brush and the smaller droplets across the jet to evaporate faster, resulting in a reduced droplet density near the edge of the jet and the survival of larger droplets downstream. From the simultaneous OH PLIF and Mie scattering measurements, structures of OH were observed within the jet, with further analysis indicating the possibility of droplets penetrating the frame front into regions with intermediate-to-high levels of OH near the downstream locations where the flame closes across the jet. Similar observations have also been reported in the literature, such as in the work by Stårner et al. [24] investigating dilute acetone spray flames. In their work, for moderate Reynolds number flows, droplets were reported to occasionally penetrate the flame front, and only for a short distance not exceeding 3 mm. This is in qualitative agreement with the averaged profiles of the normalized OH and Mie signals normal to the flame front, Fig. 14, showing very little Mie intensity after approximately 2 mm along the normal direction of the flame front towards the burned gas region. For both increasing distance downstream from the burner exit and for higher fuel loading conditions, an increasing presence of droplets in intermediate-to-high OH regions was observed from the instantaneous scatter plots of OH vs. Mie signals, and from the normalized histograms of the binary Mie vs. normalized OH, particularly for condition ES3. This would likely affect the droplet vaporization rate, which is of significance to the flame behaviour, and merits its investigation.

4.3. Droplet vaporization rate

Following the method by Pichard et al. [15], the average droplet vaporization rate, K, was estimated for the spray flame at conditions ES1 to ES3 as

$$K(z_2) = -\frac{4}{3(z_2 - z_1)}[d^3(z_2)n(z_2) - d^3(z_1)n(z_1)] \times\left(\frac{U(z_1)U(z_2)}{n(z_1)d(z_1)U(z_2) + n(z_2)d(z_2)U(z_1)}\right) \quad (4)$$

where z_1 and z_2 denote successive axial probe stations at identical radial locations across which K is evaluated, n is the droplet number density, U is the droplet axial velocity taken to equal $\langle u\rangle$ and d is the droplet diameter approximated as the Sauter Mean Diameter (SMD). A key assumption in the derivation of Eq. (4) is a constant average evaporation rate between closely spaced axial probe locations z_1 and z_2 [15]. In the present work, droplet size and velocity measurements are generally obtained at axial locations separated by a distance D = 42 mm, across which significant mean temperature changes of the fuel droplets may occur and consequently their average evaporation rate may vary. However, the assumption of a constant K between successive axial probe locations within the jet of cold reactants may still be valid where there is little influence of the flame. This can be expected for the non-reacting case (condition ES3 with pilot off) and perhaps along the centre of the jet at condition ES1. For the latter case, this is due to the relatively low heat release indicated from the weak luminosity and low OH gradients for the cylindrically shaped flame at this condition, Figs. 9 and 10, where the average flame is located at a radial distance of approximately 0.5D from the centre of the jet along the length of the imaged flame zone. However, for the spray flame at conditions ES2 and ES3, this assumption may only be valid near the centre of the jet at axial locations up to approximately 2D and 1.5D for conditions ES2 and ES3, respectively. Above this axial distance, the flame closes across the jet and both high OH gradients and OH structures are observed near the centre of the jet. One can then expect significant mean temperature differences between successive axial probe locations. Given these limitations, some useful but tentative conclusions may still be drawn from the estimates of K provided in Fig. 23.

For the non-reacting case, values of K are approximately zero near the centre of the jet along the axial locations investigated. As the boundary of the jet is approached, values of K at some axial locations increase up to approximately 0.04 mm^2/s, with larger differences in K observed between successive axial probe locations. This may indicate a departure from the assumption of constant K between successive axial probe locations near the boundary of the cold reactants jet and the ambient. For the spray flame at condition ES1, values of K remain close to zero at the centre of the jet for the axial probe locations investigated. As the flame at the jet boundary is approached, values of K increase to approximately 0.05 mm^2/s at axial locations above 1D, with larger changes observed further downstream. These observations may be expected given the relatively low heat release of the cylindrical flame brush at this very fuel lean (ϕ_{ov}) condition is not likely to have a significant effect on droplet vaporization near the centre of the jet.

At conditions ES2 and ES3, values of K near the centere of the jet at axial locations up to 2D remain near zero, and increase to approximately 0.05 mm^2/s and 0.15 mm^2/s for conditions ES2 and ES3, respectively, at further downstream locations. For condition

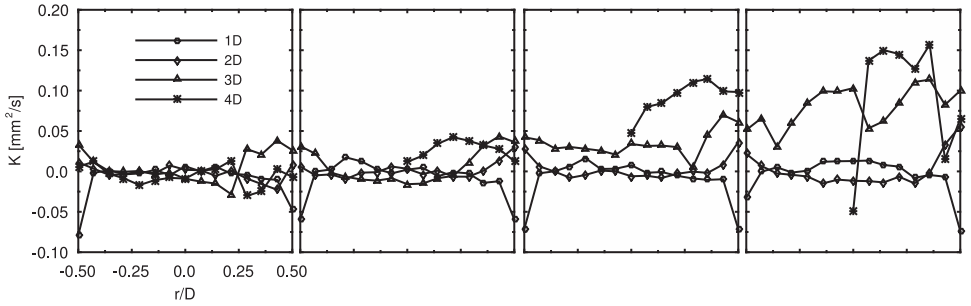

Fig. 23. Plots of the average droplet vaporization rate K for a non-reacting case (ES3 with pilot off) and for the spray flame at conditions ES1, ES2 and ES3 (columns left to right).

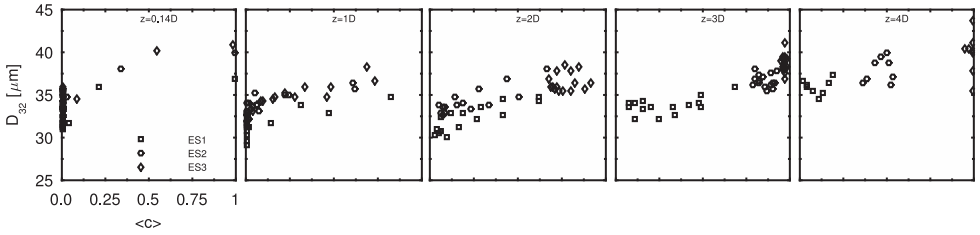

Fig. 24. Plots of SMD vs. $\langle c \rangle$ for the spray flame at conditions ES1, ES2 and ES3, for axial locations 0.14D, 1D, 2D, 3D and 4D (columns left to right).

ES2, values of K at these downstream locations show a greater increasing trend as the jet boundary is approached than for condition ES3 where a flatter profile with some scatter is observed. The closing of the flame across the jet is likely to contribute to the higher K values near the centre of the jet at these downstream locations, and higher heat release due to increased fuel loading may result in the higher overall K values near the jet boundary at higher ϕ_{ov} conditions. At condition ES3, the Mie scattering results showed no distinct jet structure past a distance 2D downstream from the burner exit, beyond which few fuel droplets survive and wide regions of low intensity OH persist, Figs. 9 and 10. This may be reflected by the absence of a trend of increasing K in the radial direction observed in Fig. 23, with droplets present at this location experiencing similar conditions of hot burned gases across the width of the imaged flame zone.

These trends generally agree with observations reported in [15]. In their work, values of K evaluated along the centre of a n-heptane droplet-air jet took on similar magnitudes (0–0.16 mm^2/s), with K shown to increase linearly with $\langle c \rangle$ estimated from binary images of OH PLIF. In the present work, the highest values of K are evaluated at the downstream locations where the flame closes across the flow, and these regions also correspond to high $\langle c \rangle$ values as shown in Fig. 15. Results reported in [15] also showed K to increase with SMD. In the present work, a small increase in SMD with fuel loading was observed, Fig. 5, presumably due to a decrease in atomization performance as the atomizing air flow rate is held constant for the conditions investigated. This may contribute to the trend of K increasing with ϕ_{ov} shown in Fig. 23. However, this contribution is likely to be small compared to that from flame-droplet interaction as the flame brush closes across the jet, which raises the mean temperature surrounding the droplets, increasing K for these high ϕ_{ov} conditions. No significant trends of droplet evaporation with the local turbulence conditions were observed, as also reported in the literature [33].

4.4. Droplet diameter and progress variable

Related to the trends discussed above on the survival of droplets in regions of high mean temperature is the relationship between the average droplet diameter and mean progress variable. The manner in which the flame brush thickness changes in a spray flame is not known, with recent studies investigating in detail the mechanisms controlling flame thickening in spray flames [13,14]. Direct Numerical Simulations of flame propagation in n-heptane droplet-air mixtures reported in [13] showed an increase in the spacing of reaction progress variable, c, isocontours with droplet diameter. In the present work, the trend of increasing SMD with Q_f also coincides with an increase in the separation of the $\langle c \rangle$ contours, Fig. 15. To investigate this further, SMD values from the PDA measurements were compared with $\langle c \rangle$ values from the OH PLIF data at interpolated probe locations of the PDA instrument within the OH PLIF imaging region. The results are shown in Fig. 24. At axial locations 0.14D and 1D from the burner exit, smaller droplets coincide with zero or low $\langle c \rangle$ values, whilst larger droplets mostly coincide with low-to-intermediate $\langle c \rangle$ values, and occasionally high $\langle c \rangle$ values. At these locations, only droplets near the jet boundary are likely to interact with the flame front. With higher SMD values observed near the boundary of the jet than at its centre at these axial locations, Fig. 5, smaller droplets predominantly located near the centre of the jet are less likely to interact with the flame than the predominantly larger droplets near the jet boundary.

At further downstream locations, OH structures are occasionally observed near the centre of the jet, and for conditions ES2 and ES3, the flame closes across the jet. Therefore, droplets of all sizes within the jet are likely to interact with the flame, particularly at conditions ES2 and ES3. One can also expect smaller droplets approaching the flame front to evaporate more readily than larger droplets which are more likely to penetrate the initial flame front and continue to evaporate in the burnt gas region of the flame. This behaviour is also observed in Fig. 24 at downstream locations $\geq$ 2D where SMD increases with $\langle c \rangle$. At these downstream locations, Fig. 24 shows smaller droplets coincide with low-to-intermediate values of $\langle c \rangle$, indicating that, on average, they are not likely to penetrate the flame front denoted by $\langle c \rangle = 0.5$. Larger droplets appear to coincide with intermediate-to-high $\langle c \rangle$ values, indicating their higher likelihood of penetrating further into the flame region prior to evaporating completely than smaller size droplets. This could lead to a thicker flame brush at these downstream locations, which would correspond to the increase in the spacing of the $\langle c \rangle$ isocontours observed in Fig. 15. However, we

again note that the average reaction progress variable signal does not indicate droplets coincide instantaneously with high reaction rate regions for the conditions investigated here.

4.5. Turbulent flame speed

At the nominal overall equivalence ratio of the experiment, the laminar flame speed of gaseous ethanol-air flames, $S_{L,g}$, is 10.4, 19.3, and 28 cm/s for conditions ES1, ES2, and ES3, respectively. In our case, we can evaluate an approximation to the turbulent flame speed as in turbulent premixed flames stabilised on burners following the definition of global consumption speed by Driscoll [17]: $S_{T,GC} = \dot{m}_R/\rho_R A_{\langle c\rangle=0.5}$. Following this definition and the $\langle c\rangle$ isolines in Fig. 15 in our case, $A_{\langle c\rangle=0.5}$ is estimated considering the $\langle c\rangle = 0.5$ isoline adjacent to the unburned reactants, and up to a maximum height of 2.4D from the burner exit. From this, we get that $S_{T,GC}$ in the present spray flames is approximately 25, 25, and 40 cm/s, respectively for conditions ES1, ES2, and ES3, respectively. With u' approximated as u_{turb}=0.15U_b from Fig. 5, the ratio $u'/S_{L,g}$ is 4.1, 2.2, and 1.5, respectively for conditions ES1, ES2, and ES3, respectively.

If the fuel were completely pre-vaporized, we could expect $S_{T,GC}/S_{L,g}$ values of approximately 2 as reported for fully premixed methane-air mixtures [17, Fig. 41]. The measured values here are 2.4, 1.3, and 1.4. These values are likely to be overestimated considering not all the fuel is consumed, particularly for condition ES1, and the flame surface area downstream is neglected for conditions ES1 and ES2 due to the inconsistency in the $\langle c\rangle$ isolines downstream. However, the values obtained for conditions ES2 and ES3 resemble the near unity values reported for n-heptane droplet-laden mixtures in [13, Fig. 2], noting however their S_T is defined as a turbulent displacement speed. In [13], values of $S_T/S_{L,g}$ for the droplet-laden mixture were shown to be lower than that of a premixed stoichiometric flame for varying levels of $u'/S_{L,g}$, which was attributed to heat absorption due to droplet evaporation reducing fuel consumption, and droplet build-up resulting in local non-flammable mixtures. More detailed measurements investigating the droplet and turbulence characteristics on the turbulent flame speed are vital for validating models of reacting turbulent droplet-laden mixtures.

5. Conclusions

Droplet size and velocity information was obtained using PDA and LDA measurements. Velocity profiles across radial sections of the jet indicate a dilute mixture of ethanol droplets uniformly dispersed in a turbulent carrier air stream. Droplet velocities conditioned on droplet size were evaluated and showed larger droplets generally have lower mean and fluctuating velocity components than smaller size droplets. Larger droplets were observed to survive further downstream where the droplet number density decreased, with stronger trends observed with higher ϕ_{ov} conditions. These trends agreed with estimates of the average droplet vaporization rate, which increased with distance downstream and higher ϕ_{ov}. Imaging of OH* chemiluminescence, OH PLIF and Mie scattering at 5 kHz and CH_2O-fuel PLIF at 5 Hz was used to study the flame-droplet behaviour. The instantaneous flame structure is relatively smooth near the burner exit, with small scale wrinkling developing with distance downstream. The mean flame shape is observed to change from cylindrical to conical as the fuel loading is increased from very lean overall conditions. Simultaneous flame and droplet imaging showed droplets rarely overlap with regions of OH. Droplets appearing to overlap generally coincide with low-to-intermediate OH values, and on occasion with high OH values. The latter primarily occurs at regions where the conical shaped flame closes across the jet, with very low droplet intensity observed past a distance 2 mm normal to the flame front in the direction of the burned gases. Statistics of the mean reaction progress variable, 2-D flame surface density and flame front curvature are evaluated and discussed with reference to the droplet size measurements. An increasing trend of droplet size with mean progress variable was observed. The flame surface density profiles near the pilot resembled those of fully premixed flames. Further downstream, their shape changes to indicate increasing flame surface in regions predominantly occupied with burned gases, with a loss in flame surface also observed to reflect the decreasing mean flame height at higher ϕ_{ov} conditions. A thicker flame brush was also observed with distance downstream, attributed to the presence of larger droplets which continue to evaporate in the burnt gas region of the flame. Higher magnitudes of flame front curvature were observed with distance downstream from the burner exit and increasing ϕ_{ov}, further indicating increasing wrinkling of the flame front downstream. The CH_2O-fuel PLIF signal was observed to qualitatively resemble the Mie scattering signal, with general trends of estimates of flame surface density and curvature based on the CH_2O-fuel PLIF signal resembling those based on the OH PLIF signal. These measurements could serve as validation data for computational models of flame propagation in simple, well defined turbulent dilute droplet-laden mixtures.

Acknowledgments

The authors gratefully acknowledge funding of this work from the EPSRC Grant EP/J021644/1.

References

[1] G. Faeth, Evaporation and combustion of sprays, Prog. Energy Combust. Sci. 9 (1983) 1–76.
[2] W. Sirignano, Fuel droplet vaporization and spray combustion theory, Prog. Energy Combust. Sci. 9 (1983) 291–322.
[3] N. Chigier, The atomization and burning of liquid fuel sprays, Prog. Energy Combust. Sci. 2 (1976) 97–114.
[4] M. Birouk, I. Gökalp, Current status of droplet evaporation in turbulent flows, Prog. Energy Combust. Sci. 32 (2006) 408–423.
[5] J. Burgoyne, L. Cohen, The effect of drop size on flame propagation in liquid aerosols, Proc. R. Soc. Lond. A 225 (1954) 375–392.
[6] S. Hayashi, S. Kumagai, T. Sakai, Propagation velocity and structure of flames in droplet-vapor-air mixtures, Combust. Sci. Tech. 15 (1977) 169–177.
[7] G. Myers, A. Lefebvre, Flame propagation in heterogeneous mixtures of fuel drops and air, Combust. Flame 66 (1986) 193–210.
[8] J. Reveillon, L. Vervisch, Analysis of weakly turbulent dilute-spray flames and spray combustion regimes, J. Fluid Mech. 537 (2005) 317–347.
[9] A. Neophytou, E. Mastorakos, Simulations of laminar flame propagation in droplet mists, Combust. Flame 156 (2009) 1627–1640.
[10] J. Gounder, A. Kourmatzis, A. Masri, Turbulent piloted dilute spray flames: Flow fields and droplet dynamics, Combust. Flame 159 (2012) 3372–3397.
[11] J. Greenberg, A. Dvorjetski, Opposed flow polydisperse spray diffusion flames: steady state and extinction analysis, Combust. Theory Model. 7 (2003) 145–162.
[12] A. Neophytou, E. Mastorakos, R. Cant, The internal structure of igniting turbulent sprays as revealed by complex chemistry DNS, Combut. Flame 159 (2012) 641–664.
[13] D. Wacks, N. Chakraborty, E. Mastorakos, Statistical analysis of turbulent flame-droplet interaction: a direct numerical simulation study, Flow Turb. Combust. 96 (2016) 573–607.
[14] D. Wacks, N. Chakraborty, Flame structure and propagation in turbulent flame–droplet interaction: a direct numerical simulation analysis, Flow Turb. Combust. 96 (2016) 1053–1081.
[15] C. Pichard, Y. Michou, C. Chauveau, L. Gökalp, Average droplet vaporization rates in partially prevaporized turbulent spray flames, Proc. Combust. Inst. 29 (2002) 527–533.
[16] F. Sacomano Filho, M. Chrigui, A. Sadiki, J. Janicka, Les-based numerical analysis of droplet vaporization process in lean partially premixed turbulent spray flames, Combust. Sci. Tech. 186 (2014) 435–452.
[17] J. Driscoll, Turbulent premixed combustion: Flamelet structure and its effect on turbulent burning velocities, Prog. Energy Combust. Sci. 34 (2008) 91–134.
[18] P. Jenny, D. Roekaerts, N. Beishuizen, Modeling of turbulent dilute spray combustion, Prog. Energy Combust. Sci. 38 (2012) 846–887.
[19] A. Karpetis, A. Gomez, An experimental study of well-defined turbulent non-premixed spray flames, Combust. Flame 121 (2000) 1–23.
[20] I. Düwel, H.-W. Ge, H. Kronemayer, R. Dibble, E. Gutheil, C. Schulz, J. Wolfrum, Experimental and numerical characterization of a turbulent spray flame, Proc. Combust. Inst. 31 (2007) 2247–2255.

[21] C. Letty, B. Renou, J. Reveillon, S. Saengkaew, G. Gréhan, Experimental study of droplet temperature in a two-phase heptane/air v-flame, Combust. Flame 160 (2013) 1803–1811.
[22] H. Rodrigues, M. Tummers, E. van Veen, D. Roekaerts, Spray flame structure in conventional and hot-diluted combustion regime, Combust. Flame 162 (2015) 759–773.
[23] E. Mastorakos, Forced ignition of turbulent spray flames, Proc. Combust. Inst. (2016).
[24] S. Stårner, J. Gounder, A. Masri, Effects of turbulence and carrier fluid on simple, turbulent spray jet flames, Combust. Flame 143 (2005) 420–432.
[25] R.C. Florea, Optical investigation of ethanol and n-heptane dual-fuel partially premixed combution in a reciprocating engine, Doctoral thesis, Wayne State University, 2012.
[26] I. Shepherd, Flame surface density and burning rate in premixed turbulent flames, Symp. (Int.) Combust. 26 (1996) 373–379.
[27] J. Kariuki, J. Dawson, E. Mastorakos, Measurements in turbulent premixed bluff body flames close to blow-off, Combust. Flame 159 (2012) 2589–2607.
[28] B. Deschamps, G. Smallwood, J. Prieur, D. Snelling, Ö. Gülder, Surface density measurements of turbulent premixed flames in a spark-ignition engine and a bunsen-type burner using planar laser-induced fluorescence, Symp. (Int.) Combust. 26 (1996) 427–435.
[29] F. Yuen, Ö. Gülder, Investigation of dynamics of lean turbulent premixed flames by rayleigh imaging, AIAA J. 47 (2009) 2964–2973.
[30] V. Weber, J. Brübach, R. Gordon, A. Dreizler, Pixel-based characterisation of CMOS high-speed camera systems, Appl. Phys. B: Lasers Optics 103 (2011) 421–423.
[31] M. Haq, C. Sheppard, R. Woolley, D. Greenhalgh, R. Lockett, Wrinkling and curvature of laminar and turbulent premixed flames, Combust. Flame 131 (2002) 1–15.
[32] A. Konnov, R. Meuwissen, L. De Goey, The temperature dependence of the laminar burning velocity of ethanol flames, Proc. Combust. Inst. 33 (2011) 1011–1019.
[33] Y.-C. Chen, S.H. Stårner, A.R. Masri, Characteristics of turbulent spray combustion in a piloted jet flame burner, Proc. Combust. Inst. 29 (2002) 625–632.
[34] R. Yuan, Measurements in swirl-stabilised spray flames at blow-off, University of Cambridge, 2015 Doctoral thesis.
[35] V. Ferrand, R. Bazile, J. Borée, G. Charnay, Gas-droplet turbulent velocity correlations and two-phase interaction in an axisymmetric jet laden with partly responsive droplets, Int. J. Multiph. Flow 29 (2003) 195–217.